Two-Magnon Raman Scattering and Exchange Interactions in Antiferromagnetic $KNiF_3$ and K_2NiF_4 and Ferrimagnetic $RbNiF_3$†*

S. R. Chinn, H. J. Zeiger, and J. R. O'Connor‡
Lincoln Laboratory, Massachusetts Institute of Technology, Lexington, Massachusetts 02173
(Received 15 June 1970; revised manuscript received 23 September 1970)

We have observed Raman scattering of 5145-Å argon-laser radiation by two-magnon excitations in the antiferromagnetic nickel fluorides $KNiF_3$ and K_2NiF_4 and ferrimagnetic $RbNiF_3$. For both the cubic perovskite structure of $KNiF_3$ and the tetragonal structure of K_2NiF_4, which behaves like a two-dimensional antiferromagnet, the experimental results are in excellent agreement with the theoretical spectra computed by a Green's-function technique. This method is reviewed for the general case of a two-sublattice Néel ferrimagnet with antiparallel spins. From a comparison with this theory, we find values of $J=70.5\pm0.8$ and 77.0 ± 2.0 cm^{-1}, respectively, for the Heisenberg exchange constants in these two materials. The experimentally observed temperature dependence of the two-magnon Raman spectra, which persists above the Néel temperature in both cases, is described. For hexagonal $RbNiF_3$, with the aid of magnon-assisted optical-absorption and magnetic-susceptibility data, we have calculated the magnon dispersion relations and estimated the dominant exchange constants. These values are 48 cm^{-1} for the antiferromagnetic 180° Ni^{2+} - F^- - Ni^{2+} superexchange interaction and 113 cm^{-1} for the 90° ferromagnetic interaction, with a small second-nearest Ni^{2+} interaction constant approximately 4 cm^{-1}. The identification of the low-temperature Raman line at 510 cm^{-1} as arising from two different Brillouin-zone-edge magnons is consistent with our exchange constants when magnon-magnon binding effects are taken into account. A Bethe-Peierls-Weiss analysis using the present exchange parameters gives a Curie temperature close to the experimental value, 139 °K, and predicts high-temperature sublattice magnetizations in good agreement with the results of nuclear-magnetic-resonance measurements. Finally, comparisons are made among these nickel fluorides, and with results found from experiments in other magnetic insulators.

I. INTRODUCTION

Recent theoretical[1-3] and experimental[4] work on Raman scattering by two magnons has shown the large effect of magnon-magnon interactions. Because of the nature of the assumed interaction mechanism of the optical radiation with the spins, the spin waves on oppositely directed sublattices are created by excitation of spins on adjacent sites. This necessarily perturbs the immediate environment seen by each of the spins from that of the normal singly excited spin state, and causes a large effect on the energy spectrum of the resultant two-magnon state. Ordinarily, in the case of independently excited spin waves at low temperatures, the spin deviations of each magnon are shared throughout the spin system and the magnons have little effect (to a first approximation) on each other. One might expect that the Raman-scattering spectrum from two-magnon excitations (with equal and opposite wave vector $\vec{k}$) would be simply the spectrum coming from the sum of the two noninteracting excitations, leading to the familiar line shape of the joint two-magnon density of states, with perhaps some wave-vector and polarization-dependent weighting factor.

Elliott *et al.*,[1-3] using a Green's-function formalism, have shown this to be incorrect, and for two-sublattice antiferromagnets they have explicitly treated the effect of the magnon-magnon interaction arising in the excitation process in Raman scattering. The resultant theory is in excellent agreement with the experimental measurements by Fleury[4] on $RbMnF_3$ with $S=\frac{5}{2}$, and with results presented below for $KNiF_3$,[5] and K_2NiF_4 with $S=1$. Similar studies have been carried out for two-magnon optical-absorption and magnon sideband spectra,[1,3,6-8] but the present work will be confined to further investigation only of Raman scattering. The most striking result is that the amplitude peak of the Raman spectrum occurs at lower energy than predicted for the noninteracting case, and the line shape is drastically altered. This can be understood physically from a simple Ising model, and as will be shown, the same qualitative features apply to the more general ferrimagnetic case.

As additional experimental verification of the Green's-function method, Raman-scattering data for the antiferromagnet $KNiF_3$ are compared with the zero-temperature theory. This provides an interesting example because it is isomorphic with $RbMnF_3$, but has $S=1$ instead of $S=\frac{5}{2}$ (which causes a difference in the Raman-scattering line shape), and has an exchange constant almost 15 times that of $RbMnF_3$. Although no quantitative theory exists for comparison with experimental results at high temperatures, it is interesting to note the persistence of scattering from the magnetic excitations in

$KNiF_3$ up to at least 300 °K, or $1.2T_N$.

Another system for which experimental data are presented is K_2NiF_4. This compound is similar in many ways to $KNiF_3$ but the additional layers of KF in its crystal structure give rise to two-dimensional antiferromagnetic behavior. A simple modification of the Green's-function calculation for two-dimensional systems yields excellent agreement with the low-temperature two-magnon Raman spectrum observed for this material. As in $KNiF_3$, this spectrum persists up to and above the magnetic ordering temperature.

The third nickel fluoride which we have studied is $RbNiF_3$. This hexagonal magnetic insulator has been the subject of a number of experimental studies in the last few years because of its unusual properties. This material is transparent and ferrimagnetic with a transition temperature of 139 °K. A preliminary report and analysis of two-magnon Raman scattering in $RbNiF_3$ has been given by Chinn *et al.*[9,10] and Fleury *et al.*[11]

The study of two-magnon scattering in $RbNiF_3$ is of special interest because the results can be compared and contrasted with those obtained in antiferromagnetic $KNiF_3$. As will be discussed later in more detail, the local Ni^{2+} environment in $RbNiF_3$ is very much like that in the perovskite $KNiF_3$, but the Ni^{2+}-$6F^-$ octahedra are arranged to give a six-layer structure with a net magnetic moment in the ground state.

The present experimental results of Raman scattering in $RbNiF_3$ show an intense broad peak, shifted approximately 510 cm^{-1} from the excitation energy. As in the scattering from $KNiF_3$, this line also broadened and its shift decreased as the sample temperature increased. From the experimental evidence, we interpret this line as a two-magnon excitation.

Because of the lower symmetry of this crystal, the $RbNiF_3$ spin-wave spectrum is much more complex than that of $KNiF_3$. The Green's-function calculation for the interacting two-magnon Raman-scattering line shape, which was feasible in the case of $KNiF_3$, is impractical for $RbNiF_3$. We are forced to start from a free-magnon description, and include the magnon interaction effects in a flat-band approximation. The correction is large and improves significantly the agreement of the observed frequency of the two-magnon Raman-scattering peak, with the value predicted from exchange constants obtained from an analysis of other experiments.

In Sec. II, we present a summary of the results of the Green's-function method for the general case of the two-sublattice Néel ferrimagnet. We treat this extension of the particular case of the simple antiferromagnet to examine the effects, if any, of a net magnetic moment in the magnetic ground state, and to establish a notation for the later comparison with experiments. We shall use the antiferromagnetic results for $KNiF_3$ and K_2NiF_4; the more general solutions will be of particular interest for ferrimagnetic $RbNiF_3$. In Sec. III, the experimental two-magnon Raman-scattering results for $KNiF_3$ are compared with the predictions of the Green's-function theory, and in Sec. IV, a similar comparison is made for K_2NiF_4. In Sec. V, a summary of the magnetic properties of $RbNiF_3$ is given. Section VI presents the experimental two-magnon scattering results. In Sec. VII, the spin-wave spectrum for $RbNiF_3$ is obtained. The comparison of the spin-wave theory with the results of magnon sideband and susceptibility experiments yields a set of exchange constants for $RbNiF_3$. These constants are shown to provide a reasonable explanation of the two-magnon scattering results. In Sec. VIII, to provide further confirmation of these values, detailed Bethe-Peierls-Weiss (BPW) calculations are carried out. Using these exchange constants, the BPW calculations are shown to give good agreement with the results of NMR experiments, with no further adjustable parameters. Finally in Sec. IX, our experimental results are discussed in the light of other measurements in these materials, and comparisons among $KNiF_3$, K_2NiF_4, and $RbNiF_3$ are made.

II. REVIEW OF GREEN'S-FUNCTION METHOD

A. Raman Interaction and Exchange Hamiltonians

The mechanism for scattering of electromagnetic radiation by magnetic excitations has been examined in detail by several authors,[12–17] and we shall only summarize their results for the case of particular interest. In two-magnon Raman scattering an interionic electronic off-diagonal exchange coupling of the radiation field with the spins is probably most important, although in one-magnon processes, where such an interaction cannot play a role, a spin-orbit coupling mechanism probably predominates. Taking into account the exchange mechanism with a spin-only ground state, the spin-dependent polarizability tensor simplifies to

$$\alpha_{jl}^{\mu\nu} = B_{jl}^{\mu\nu}\,\vec{S}_j \cdot \vec{S}_l \,, \tag{1}$$

which leads to a Raman-scattering Hamiltonian

$$H_{\text{Raman}} = \sum_{\mu\nu;jl} E_\mu E'_\nu B_{jl}^{\mu\nu}\,(\vec{S}_j \cdot \vec{S}_l) \,. \tag{2}$$

Here, E_μ and E'_ν are the incident and scattered electric field components which cause Raman scattering at the difference frequency $\pm(\omega - \omega')$. A physical interpretation of the Stokes-scattering process is that the incident photon excites one electron to a virtual state, with simultaneous spin flip of it and

a neighboring electron (to conserve spin angular momentum). The excited electron then returns to the orbital ground state emitting the scattered photon, and leaving both spins excited.

This type of scattering interaction should predominate in systems with antiparallel spins, where the matrix elements of S^+S^- are large. In ferromagnets or systems with parallel spins, at low temperatures such terms would be small, and other mechanisms such as the spin-orbit interaction taken to second order would have to be invoked. We shall examine only the exchange-scattering mechanism and therefore restrict our attention to ferrimagnetic systems in which neighboring spins are approximately antiparallel. In particular, because of the simplicity of analysis and its later application to real crystals exhibiting cubic and square symmetry, we shall examine the scattering problem for the case of the cubic perovskite lattice.

The tensor $\underline{B}$ must have the symmetry of the lattice, and for the perovskite structure we take the scattering Hamiltonian given by Thorpe and Elliott, [2]

$$H_{\text{Raman}}=\sum_{\vec{j},\vec{n}}\left[B_1(\vec{E}\cdot\vec{E}')+B_3\left(\frac{\vec{E}\cdot\vec{E}'}{3}-\frac{(\vec{E}\cdot\vec{n})(\vec{E}'\cdot\vec{n})}{n^2}\right)\right]\times\vec{S}_{\vec{j}}\cdot\vec{S}_{\vec{j}+\vec{n}}\,, \tag{3}$$

where $\vec{n}$ is a nearest-neighbor vector connecting up and down spins.

For the exchange Hamiltonian of the system we use a simple modification of an antiferromagnetic Hamiltonian, namely,

$$H_{\text{spin}}=\sum_{\vec{j},\vec{n}} J(\vec{n})\vec{S}_{\vec{j}a}\cdot\vec{S}_{\vec{j}+\vec{n},b}+A(\vec{n})S^x_{\vec{j}a}\,S^x_{\vec{j}+\vec{n},b}\,. \tag{4}$$

Here $J(\vec{n})$ is the positive isotropic exchange between sites labeled by $\vec{j}$ on the up sublattice a and sites labeled by $j+n$ on the down sublattice b. The term $A(\vec{n})$ is the corresponding anisotropic exchange constant. By choosing this particular example, we neglect the unessential features of single-ion anisotropy and examine the possible consequences for Raman scattering of having a net moment in the antiparallel ferrimagnetic ground state. The effects of single-ion anisotropy can be included in a simple fashion, and we shall describe their effects for the specific experimental examples discussed below. Including the anisotropic exchange term in Eq. (4) allows us to pass to the limiting case of the Ising model which will give a physical semiquantitative insight into the magnon-interaction problem. In the Hamiltonians (3) and (4) and in the remainder of this paper we shall consider only nearest-neighbor interactions. We impose this restriction not from theoretical limitations of the Green's-function method but for convenience in the numerical computations. Furthermore, this is probably an excellent approximation for our actual experimental examples.

The spin-wave modes and energies are found by solving the equations of motion for the magnon excitation operators. After making a Holstein-Primakoff transformation, the usual linear approximation, and a standard Bogolyubov transformation, [18] we have the dynamic part of the spin Hamiltonian in the diagonal form with normal-mode creation and annihilation operators,

$$H_{\text{spin}}=\sum_{\vec{k}}\lambda_{\vec{k}}\,\alpha^\dagger_{\vec{k}}\alpha_{\vec{k}}+\mu_{\vec{k}}\,\beta^\dagger_{\vec{k}}\beta_{\vec{k}}\,. \tag{5}$$

The eigenvalue equations for $\lambda_{\vec{k}}$ and $\mu_{\vec{k}}$ give

$$\lambda_{\vec{k}}=\frac{S_b-S_a}{2}\left[J(0)+A(0)\right]\left[1+\left(1+\frac{4S_aS_b(1-\gamma^2_{\vec{k}})}{(S_b-S_a)^2}\right)^{1/2}\right],$$

$$\mu_{\vec{k}}=\frac{S_b-S_a}{2}\left[J(0)+A(0)\right]\left[\left(1+\frac{4S_aS_b(1-\gamma^2_{\vec{k}})}{(S_b-S_a)^2}\right)^{1/2}-1\right], \tag{6}$$

$$J(\vec{k})=\sum_{\vec{n}}J(\vec{n})\,e^{i\vec{k}\cdot\vec{n}}\,,\quad A(\vec{k})=\sum_{\vec{n}}A(\vec{n})\,e^{i\vec{k}\cdot\vec{n}}\,.$$

We have assumed $S_b\geq S_a$, and have defined $\gamma_{\vec{k}}=J(\vec{k})/[A(0)+J(0)]$. The mode with energy $\lambda_{\vec{k}}$ is the upper "optical" mode and that with $\mu_{\vec{k}}$ is the lower "acoustic" mode, after the analogous phonon modes. Near the Brillouin-zone boundaries the excitations occur mainly on separate sublattices, and near the zone center they are shared more between the sublattices.

In the case of $S_b=S_a$, the simple antiferromagnet, the above results yield the well-known antiferromagnetic dispersion relations and mode strengths, as the limit $S_b\to S_a$ is taken in Eq. (6).

For the limiting case of the Ising model, the isotropic exchange J vanishes, leaving only the z-z exchange component A. There is no dispersion, and the two modes, confined on their respective sublattices, have energies $A(0)S_a$ and $A(0)S_b$, which correspond to the zone-boundary magnon energies for the Heisenberg model. Because of its particularly simple nature, and δ-function density of states not too dissimilar from the actual physical case, this Ising model will be useful later in an approximation to the Green's-function calculation.

B. Scattering Cross Section and Green's-Function Calculation

The two-magnon Raman-scattering cross section is found from the Fourier transform of a sum of spin pair-pair correlation functions

$$\frac{d^2\sigma}{d\omega d\Omega}\propto\sum_{\vec{j}\vec{j}';\mu\nu}\int_{-\infty}^{\infty}e^{-i\omega t}\,dt$$

$$\times\langle\sum_{\vec{n}} B^{\mu\nu}(\vec{n})\vec{S}_{\vec{j}a}(t)\cdot\vec{S}_{\vec{j}+\vec{n},b}(t)$$

$$\times\sum_{\vec{n}'} B^{\mu\nu}(\vec{n}')\vec{S}_{\vec{j}',a}(0)\cdot\vec{S}_{\vec{j}'+\vec{n}',b}(0)\rangle\ . \qquad (7)$$

The essential transformed correlation functions which comprise this cross section are simpler in form and are written as

$$C(\vec{n},\vec{n}')\equiv\langle\sum_{\vec{j}}\vec{S}_{\vec{j}a}(t)\cdot\vec{S}_{\vec{j}+\vec{n},b}(t)$$

$$\times\sum_{\vec{j}'}\vec{S}_{\vec{j}',a}(0)\cdot\vec{S}_{\vec{j}'+\vec{n}',b}(0)\rangle_{\omega}\ , \qquad (8)$$

where the subscript ω denotes the Fourier frequency component from Eq. (7). The technique of finding the correlation functions or cross section by the Green's-function method is well known[19] and is summarized by Elliott and Thorpe.[3] Since the results for our simple model are quite similar, we shall not repeat their derivation but indicate only the differences in the final results.

In evaluating the total cross section using the scattering Hamiltonian (3), we see that there are two linear combinations of $C(\vec{n},\vec{n}')$ transforming like Γ_1^+ and Γ_3^+ whose symmetry allows Raman scattering. The Γ_1^+ mode is the uniform summation over nearest neighbors $\sum_{\vec{n},\vec{n}'} C(\vec{n},\vec{n}')$. The equation of motion for the corresponding Green's function will then depend on

$$[\sum_{\vec{j},\vec{n}}\vec{S}_{\vec{j}a}\cdot\vec{S}_{\vec{j}+\vec{n},b}\ ,\ H_{\rm spin}]\ ,$$

and since this combination of $\vec{S}_{\vec{j}a}\cdot\vec{S}_{\vec{j}+\vec{n},b}$ is proportional to $H_{\rm spin}$ in the nearest-neighbor approximation, the commutator vanishes and no Γ_1^+-mode scattering is found.

The remaining part of the Green's-function calculation is very similar to that of Ref. 3. For simplicity, only the transverse parts of the spin dot products in Eq. (8) are considered. As discussed in Ref. 3 and verified by an approximate numerical calculation,[20] the most important effects of the $S_a^z S_b^z$ terms are felt in the Γ_1^+ mode, which vanishes anyway, so that the Γ_3^+ mode is accurately found with only the transverse spin components.

After solving the Green's-function equations of motion, using the Néel state for the matrix elements in the inhomogeneous terms, we find the Γ_3^+ combination of the Green's function

$$G(\vec{n},\vec{n}',E)\equiv\langle\langle\sum_{\vec{j}} S_{\vec{j}a}^{+}S_{\vec{j}+\vec{n},b}^{-}+S_{\vec{j}a}^{-}S_{\vec{j}+\vec{n},b}^{+}\ ;$$

$$\times\sum_{\vec{j}'} S_{\vec{j}',a}^{+}S_{\vec{j}'+\vec{n}',b}^{-}+S_{\vec{j}',a}^{-}S_{\vec{j}'+\vec{n}',b}^{+}\rangle\rangle \qquad (9)$$

to be

$$G(\Gamma_3^+)=\frac{4NS_aS_b(2\mu-J-A)H^0(\Gamma_3^+)}{\pi[1+(J+A)(4\mu-J-A)H^0(\Gamma_3^+)]}\ . \qquad (10)$$

In this equation

$$2\mu=[J(0)+A(0)](S_a+S_b)$$

and

$$H^0(\Gamma_3^+)=\frac{1}{N}\sum_{\vec{k}}\frac{(\cos k_x a-\cos k_y a)^2}{E^2-(\lambda_{\vec{k}}+\mu_{\vec{k}})^2}\ .$$

The perfect-lattice Green's function $H^0(\Gamma_3^+)$ has poles at the unperturbed two-magnon energies $(\lambda_{\vec{k}}+\mu_{\vec{k}})$, and would give the scattering cross section in the absence of the magnon-magnon interaction, which has been included through the decoupling of the equations of motion. These expressions are similar to those given in Eqs. (7.2) and (7.5) of Ref. 3, with the following replacements:

$$S^2\to S_aS_b\ ,\quad 2S\to S_a+S_b\ ,\quad 2E_{\vec{k}}\to\lambda_{\vec{k}}+\mu_{\vec{k}}\ . \qquad (11)$$

The spectrum of the scattered radiation is proportional to $-\mathrm{Im}G(\Gamma_3^+)$, and the resonant denominator in Eq. (10) causes a peak in intensity at a sideband energy lower than that predicted for the noninteracting case located at $[J(0)+A(0)](S_a+S_b)$.

In the numerically simpler case of isotropic exchange ($A=0$), $H^0(\Gamma_3^+)$ can be converted to the integral form

$$\frac{1}{N}\sum_{\vec{k}}\frac{e^{i\vec{k}\cdot(\vec{n}-\vec{n}')}}{E^2-(\lambda_{\vec{k}}+\mu_{\vec{k}})^2}=(i)^{p+q+r+1}\left(\frac{3}{2\mu}\right)^2\frac{S_a+S_b}{4S_aS_b}\frac{1}{\mathcal{E}}$$

$$\times\int_0^{\infty}e^{-i\mathcal{E}t}J_p(t)J_q(t)J_r(t)\,dt\ , \qquad (12)$$

where $J_m(t)$ is an mth-order Bessel function, $n-n'=a(p,q,r)$ with p, q, and r integers, and

$$\mathcal{E}=\frac{3}{2}\frac{S_a+S_b}{(S_aS_b)^{1/2}}\left[1-\left(\frac{E}{2\mu}\right)^2\right]^{1/2}\ .$$

We have numerically recalculated these integrals (tabulated in Refs. 21–23) over smaller intervals of $\mathcal{E}$, and computed the theoretical Raman spectra for various values of S_a and S_b as a function of the normalized energy. Some typical results are shown in Fig. 1, along with the unperturbed noninteracting spectra.

The major consequence of having $S_a\neq S_b$ is to increase the minimum energy in the Raman sideband from $E=0$ (in the absence of anisotropy) to $E=J(0)\times|S_a-S_b|$. In comparing this case with an antiferromagnet, apart from this large energy gap, the difference in spin magnitude and presence of a ground-state moment in the ferrimagnet has little effect on the two-magnon Raman spectrum. This

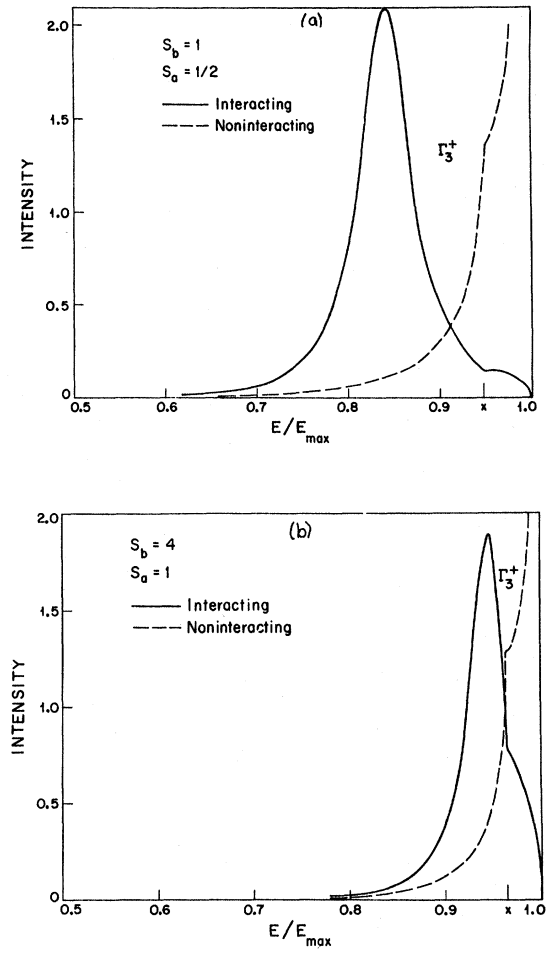

FIG. 1. Two-magnon theoretical Raman spectra (using only transverse spin components in the scattering interaction) for interacting and noninteracting magnons as a function of normalized energy in the perovskite ferrimagnet: (a) $S_b=1$, $S_a=\frac{1}{2}$; (b) $S_b=4$, $S_a=1$.

result has little bearing for the two antiferromagnetic examples discussed below, but is an important qualitative result for the ferrimagnet $RbNiF_3$ described later.

The simple physical explanation of these effects given by the Ising model for antiferromagnets also holds in the general case. The effect of exciting adjacent spins is to lower the pair excitation energy by an amount A. This can be seen in another way by use of the above Green's-function formalism with the Ising-model perfect-crystal Green's function

$$G = \frac{1}{E^2 - [A(0)(S_a + S_b)]^2} .$$

As Thorpe[24] has shown, this approximation becomes less accurate in cases such as MnF_2, where the Heisenberg perfect-crystal density of states is broad or has several peaks.

The results of this section are valid for any S_a and S_b. In the special case of the antiferromagnet with $S_a = S_b$, all of the findings are directly applicable. Single-ion anisotropy can be included and the slight modifications will be given in Sec. III, which describes the results for $KNiF_3$. Another interesting special case covered by this theoretical treatment is the two-dimensional square antiferromagnetic lattice. Again, all of the general results hold, with the only differences coming from the smaller number of nearest neighbors, the details of the symmetrical linear combinations of Green's functions, and the two-dimensional summations over $\vec{k}$ space. These modifications will be described for the particular case of K_2NiF_4.

III. $KNiF_3$: AN $S = 1$ ANTIFERROMAGNETIC PEROVSKITE

A. Introduction

As a special case of the ferrimagnets, we shall treat the $S=1$ perovskite antiferromagnet, with $S_a = S_b$, and compare the theoretical Raman spectrum with experimental results obtained for $KNiF_3$. This compound is of interest because it is isomorphic with $RbMnF_3$, which has $S=\frac{5}{2}$ and furnished the first experimental confirmation[4] of the Green's-function theory for magnon-magnon effects in optical scattering. In addition, the Ni^{2+}-F^--Ni^{2+} superexchange interaction is much stronger than that of Mn^{2+}-F^--Mn^{2+}, and causes a two-magnon Raman shift of over 800 cm^{-1}, the largest yet reported. Infrared absorption measurements[25] on $KNiF_3$ have indicated a large anisotropy gap, in contrast to $RbMnF_3$, which has a negligible anisotropy field,[26] and the effects of a $\vec{k}=0$ gap in $KNiF_3$, while small, can be included in the evaluation of the experimental data. Finally, because of its smaller spin, the possibility of observing larger effects of zero-point deviations from the Néel state is considered. Although no quantitative theory exists, experimental results are also presented at higher temperatures, up to $1.2T_N$, at which the magnetic scattering is still seen.

B. Experimental Procedure

To prepare ABF_3 compounds, it is desirable, prior to crystal growth, to obtain stoichiometric materials. Starting material was obtained by using a double-decomposition technique, according to the reaction

$$3KF + NiCl_2 \rightarrow KNiF_3 + 2KCl .$$

The components were then heated in a graphite crucible to 1000 °C, slowly cooled, and then dissolved in water. Crystals were dried by conven-

tional techniques.

Crystal growth was accomplished by loading a graphite crucible with material obtained by the double-decomposition method. The crucible was contained in a sealed nickel crucible, with provision for adding a small amount of NH_3HF_2. This assembly was placed in an rf field and brought to growth temperature. The nickel crucible was slowly passed through a sharp temperature gradient to provide optimum growth conditions.

Standard Raman-scattering techniques were used. The optical excitation was 5145-Å polarized light from an argon-ion laser. Radiation at 4880 Å was also tried, but was absorbed more strongly and gave a weaker Raman signal. The laser power output was approximately 500 mW. The sample was mounted in a variable-temperature Dewar and was maintained at a constant temperature by a regulated flow of cold helium gas and by a feedback-controlled electric heater in the sample mount. A calibrated platinum thermometer measured temperatures above 20 °K and a germanium thermometer was used at lower temperatures. Measurements were accurate to within 1 °K.

Light scattered from the sample at 90° from the incident direction was collected by lenses and focused on the entrance slit of a $\frac{1}{4}$-m Ebert grating monochromator. The filtered light from this instrument was focused into a Littrow grating monochromator, whose wavelength drive was mechanically linked to that of the foregrating instrument. This combination was used in order to decrease the intensity of the scattered light at the laser wavelength. At the exit slit of this spectrometer the light was focused onto the photocathode of a photomultiplier having a S-20 response. The dark output pulses from this tube were amplified, amplitude discriminated, shaped, and counted. The dark count rate was approximately 5 per second. The output pulses were also filtered and fed into a strip-chart recorder which recorded the Raman-scattering signal intensity as the spectrometer wavelength was electrically swept. When the polarization properties of the scattering were examined, a half-wave plate was inserted into the laser beam to rotate the plane of linear polarization, and the scattered light passed through a Polaroid filter.

C. Theoretical Raman Spectrum and Experimental Results

The Green's-function theory for $KNiF_3$ can be obtained either as a special case of the ferrimagnet considered above or directly from the treatment by Elliott and Thorpe.[1-3] As they have shown, the effects of anisotropy can be included in a simple manner, and we shall use their notation. If the single-ion anisotropy is included in the form

$$H_{An} = -D\sum_{\vec{j}}[(S_{\vec{j}}^z)^2 + (S_{\vec{j}+\vec{n}}^z)^2] - H_A\sum_{\vec{j}}(S_{\vec{j}}^z - S_{\vec{j}+\vec{n}}^z)\,, \quad (13)$$

then all previous results hold, with the following changes:

$$\mu = S[J(0) + A(0) + H_A + D(2S-1)]\,,$$
$$E_{\vec{k}}^2 \equiv \lambda_{\vec{k}}^2 = \mu_{\vec{k}}^2 = \mu^2 - S^2J^2(\vec{k})\,. \quad (14)$$

In the present case, we shall assume that the exchange is completely isotropic, and for notational simplicity, include all the anisotropy effects in one term H_A. Then, in terms of the original $\mu_0 = SJ(0)$,

$$E_{\vec{k}}^2 = \mu_0^2[(1+\Delta)^2 - \gamma_{\vec{k}}^2]\,, \quad \Delta \equiv H_A/J(0)\,, \quad (15)$$

and in Green's-function argument, $\mathcal{E} = [(1+\Delta)^2 - (E/2\mu_0)^2]^{1/2}$. The only major effect on the spectrum for small Δ is to raise the lower limit of the Raman sideband energy from $E=0$ to $E = 2\mu_0 \times [2\Delta + \Delta^2]^{1/2}$, twice the anisotropy gap at $\vec{k}=0$. The theoretical line shape for the Γ_3^+ mode for $S=1$ with $\Delta = 0$ is shown in Fig. 2.

The experimental Raman spectrum of $KNiF_3$ obtained at 5 °K with 5145-Å light is also shown in Fig. 2. The sample was unoriented and no polarization analysis was done on this spectrum. In other measurements on the same sample, the $\parallel$ and $\perp$ scattering configurations were observed (i.e., $\vec{E} \parallel \vec{E}'$ and $\vec{E} \perp \vec{E}'$, respectively) with no apparent change in the spectral line shape. Since the Γ_1^+ mode is not excited when $\vec{E}\cdot\vec{E}' = 0$, and the Γ_3^+ mode is excited with both $\vec{E} \parallel \vec{E}'$ and $\vec{E} \perp \vec{E}'$, this experimental result means that the uniform mode was not observable. This finding is in agreement with the theoretical prediction of Sec. I.

Superimposed on the experimental data in Fig. 2

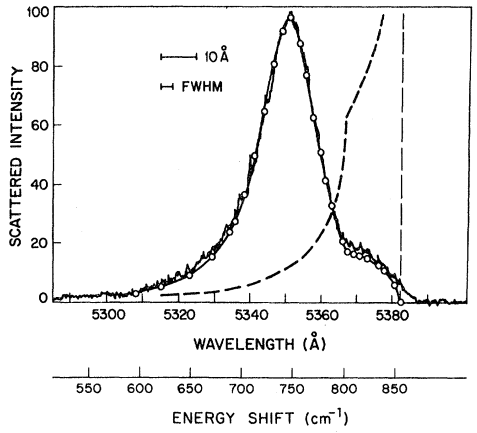

FIG. 2. Experimental and theoretical two-magnon Raman spectra as a function of wavelength for $KNiF_3$ at 5 °K with 5145-Å excitation. The dashed line is the noninteracting magnon spectrum, and the heavy solid line with circles is the computed interacting magnon spectrum.

is the theoretical curve obtained by taking $J = 71.0 \pm 0.8\ \mathrm{cm}^{-1} = (102.2 \pm 1.2)\ ^\circ\mathrm{K}$ and $\Delta = 0$. As is seen, the agreement between the Green's-function theory and experiment is quite good. To take the anisotropy into account, the maximum energy, $12J + 2H_A$, was chosen to be $852\ \mathrm{cm}^{-1}$, the maximum of the best-fitted curve with $\Delta = 0$. The additional information of the $\vec{k} = 0$ splitting, $48.7\ \mathrm{cm}^{-1}$,[25] found from antiferromagnetic resonance absorption in the infrared, gives $(48.7)^2 = 12JH_A + H_A^2$. Simultaneous solution gives $H_A = 2.79\ \mathrm{cm}^{-1} = 4.15\ ^\circ\mathrm{K}$ and $J = 70.5\ \mathrm{cm}^{-1} = 101.5\ ^\circ\mathrm{K}$, or $\Delta = 0.0066$. The theoretical spectrum with these parameters was computed and was nearly indistinguishable from Fig. 2 in the region shown. In one sense, this is an advantageous feature, since a good estimate for J can be obtained even with little knowledge of H_A. It is not clear what might cause such a large anisotropy in this material, since the cubic crystal structure should give little anisotropy from crystal field or dipolar contributions. In any event the question is not too serious here since the value of J changes by only 0.7%, depending on whether or not the anisotropy effect is included.

The two-magnon Raman spectrum was also observed as a function of temperature. As temperature increased, the higher-energy bump and slope change, characteristic of the interaction effect and X critical point, gradually became indistinct, the line broadened, its amplitude decreased, and the energy shift of the line peak decreased. A plot of the peak position and half-width is shown in Fig. 3. Although the graphs stop at $T_N = 253\ ^\circ\mathrm{K}$,[27] because it was difficult to measure accurately a linewidth or peak, there was definite evidence of a broad weak spectrum remaining up to and beyond $300\ ^\circ\mathrm{K}$, 1.2 times the Néel temperature.

Even at the higher temperatures, the maximum energy shift in the Raman spectrum remained very close to its low-temperature value. In the high-temperature region, it would seem to be more physically reasonable to picture the excitations as being localized and coming from regions with short-range spin correlation. Since the zone-edge magnons which predominate in the scattering process have very short wavelength, it is also possible to think of the excitations as being very highly damped magnons. Fleury[4,28] discusses this for the case of NiF_2, in which two-magnon Raman scattering also persisted above the ordering temperature.

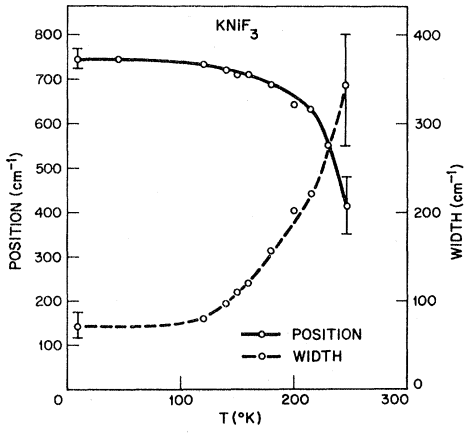

FIG. 3. Experimentally measured peak position and linewidth (full width at half-maximum) of the two-magnon Raman line in $KNiF_3$ as a function of temperature.

At first glance, one might be tempted to apply the random-phase-approximation (RPA) decoupling scheme in the above Green's-function theory at nonzero temperatures and make the appropriate replacement of S^z operators by their thermal average. This would lead to some qualitatively correct results, such as the decrease in the Raman shift of the line peak, a broadening, and decrease in amplitude. However, there remains a serious drawback in this scheme because the magnon energies are renormalized, and decrease as the temperature increases. This has the effect of decreasing the maximum energy in the Raman spectrum, and in fact would give zero energy shift at T_N. Such behavior is markedly different from the experimental evidence that the maximum energy does not change with temperature, so that a better procedure for solving and decoupling the Green's-function equations is needed at high temperatures. It is possible to use a local molecular-field model to estimate the nearest-neighbor correlation function at higher temperatures. Assuming that the energy at the peak of the Raman spectrum is proportional to this correlation, we have

$$E_{\mathrm{Raman}}(T_N) \simeq 400\ \mathrm{cm}^{-1} \simeq -11J\langle \vec{S}_j \cdot \vec{S}_{j+\vec{n}} \rangle_{T_N} ,$$

where we have approximated the effects of the magnon-magnon interaction by subtracting one nearest-neighbor interaction. This calculation gives

$$\langle \vec{S}_j \cdot \vec{S}_{j+\vec{n}} \rangle_{T_N} \simeq -0.52 ,$$

which implies that considerable short-range order exists even at the Néel temperature.

IV. K_2NiF_4

A. Two-Dimensional Antiferromagnet

Another magnetic insulator which we have investigated experimentally and by means of the Green's-function theory is the antiferromagnet K_2NiF_4.[29] This compound is of interest for several reasons, most notably because it behaves like a two-dimensional (henceforth abbreviated as [2]) Heisenberg antiferromagnet.[30] In fact, K_2NiF_4 is one of a class of such magnetic compounds, and it and its isomorphs such as Rb_2MnF_4, K_2MnF_4, Rb_2FeF_4, and

Rb_2CoF_4 have recently been the subject of much experimental and theoretical study.[27,30a,30–39]. A brief review article by Lines[40] summarizes the theory and early experimental work in magnetism in two dimensions. After completing the present work, we became aware of a recent theoretical treatment by Parkinson[41] of the optical properties of antiferromagnets with the K_2NiF_4-layer structure. The material K_2NiF_4 is also interesting because of its similarity to the perovskite $KNiF_3$, which we have just discussed. A thorough comparison of these two compounds has been made, [27] and from the Raman-scattering measurements we present additional experimental data, particularly for the exchange constants, to extend this comparison.

The structures of K_2NiF_4 and $KNiF_3$ are shown in Fig. 4. In K_2NiF_4, the perovskitelike layers of $KNiF_3$ are separated by planes of KF. The result of these additional KF layers and the lattice symmetry is a very small intraplanar interaction. A recent investigation of neutron scattering in K_2NiF_4 [36] indeed showed that the intraplanar nearest-neighbor exchange constant J is more than 270 times as large as the interplanar constant J'. As Lines pointed out, [27] the fact that a given Ni^{2+} spin has four symmetrically located Ni^{2+} neighbors in an adjacent plane actually tends to inhibit order between adjacent planes. The presence of this feature and uniaxial anisotropy along the c axis (which is necessary for [2] long-range order) thus make K_2NiF_4 an excellent approximation to a [2] Heisenberg system. Measurements of the temperature dependence of the elastic neutron scattering[30,35] confirm the [2] properties of K_2NiF_4. The temperature at which both [2] and [3] order occur is 97.1 °K. As described in Refs. 35 and 36, the phase transition is essentially [2] in character and the magnons also behave like [2] excitations. The [3] ordering follows as a consequence of long-range order within the planes, and the [3] aspects of the transition are superfluous.

In the following sections we describe the Raman-scattering experimental procedures and data for K_2NiF_4. After brief discussion of the phonon spectrum, the experimentally observed two-magnon Raman scattering is compared with the [2] modification of the Green's-function theory presented for $KNiF_3$. Our theoretical discussion of the [2] two-magnon Raman spectrum is like that of Parkinson, with the only difference arising from our use of different types of tables for the numerical evaluation of Green's-function integrals and our explicit presentation of results for $S = 1$. Although the measurements of the temperature dependence of the two-magnon scattering are not as quantitative as in $KNiF_3$, we present a qualitative description of its behavior in the temperature range 5–150 °K.

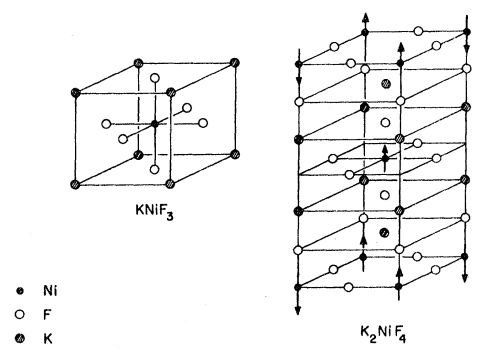

FIG. 4. Crystal structures of $KNiF_3$ and K_2NiF_4.

B. Experimental Procedure

The experimental study of Raman scattering in K_2NiF_4 was carried out in the same manner and with the same apparatus as described previously in the investigation of $KNiF_3$. The optical excitation had a wavelength of 5145 Å, with about 500 mW of power. The main difference in this experiment arose from the poorer optical quality of the K_2NiF_4 sample.

The compound K_2NiF_4 exists as a single-phase material but undergoes a peritectic transformation at ~ 930 °C. As such, crystals of this material cannot be grown directly from the melt. In order to obtain reasonably good optical-quality material, a KF liquid layer was slowly passed through a K_2NiF_4 polycrystalline charge. The KF molten layer was maintained at 900 °C. The K_2NiF_4 crystal is slowly precipitated from the KF-rich solution. The sample used was approximately 5 mm on a side, and was cut from the crucible-grown boule. Analysis of material from this boule by x-ray powder photographs showed that the composition was indeed K_2NiF_4, with no noticeable (< 3%) phases of $KNiF_3$ or KF which can easily occur during growth.

The boule was not a single crystal, and had many visible faults and cracks which were aligned primarily along its cylindrical axis. As a result, the cubic sample had a large amount of spurious elastic scattering of the incident laser beam, and it was particularly difficult to transmit the laser beam through the sample perpendicular to the direction of the faults. Unfortunately, the highest magnon scattering intensities were observed in this configuration, with a signal-to-noise ratio of only about 3 to 1. Although the laser beam was directed through the sample as close as possible to the parallel side face which was being observed, we estimate that the Raman signal strength was reduced at least an order of magnitude by the attenuating and scattering effects of the sample's flaws.

C. Theoretical Raman Spectrum and Experimental Results

Before discussion of the two-magnon Raman scat-

tering in K_2NiF_4, we shall briefly mention the phonon Raman scattering which was also observed. In the cubic perovskite $KNiF_3$ the optical-phonon modes were not Raman active and only the magnetic excitations were observable. In K_2NiF_4, with space-group symmetry[34] D_{4h}^{17}, the crystal symmetry is no longer cubic, and some of the optical-phonon modes are Raman active. From a group-theoretical analysis there should be $2A_{1g}+2E_g$ modes observable by Raman scattering. Two strong modes at energies approximately 172 and 382 cm^{-1} were seen over the entire temperature range examined. Because of the poor sample quality, no polarization analysis was possible in order to determine the symmetry of these phonons.

The Green's-function theory for two-magnon scattering in K_2NiF_4 is a simple modification of that for $KNiF_3$. The same form of nearest-neighbor bor spin Hamiltonian with anisotropy is used,

$$H_s=\sum_{\vec{j},\vec{n}} J(\vec{n})\vec{S}_{\vec{j}}\cdot\vec{S}_{\vec{j}+\vec{n}}-D\sum_{\vec{j}}[(S_{\vec{j}}^z)^2+(S_{\vec{j}+\vec{n}}^z)^2]$$

$$-H_A\sum_{\vec{j}}(S_{\vec{j}}^z-S_{\vec{j}+\vec{n}}^z)\,, \tag{16}$$

and we assume that spins in different NiF_2 planes do not interact. This effectively separates the system into many independent [2] systems which can be treated separately. After including all the anisotropy terms in the effective-field parameter H_A, the [2] magnon energies are

$$E_{\vec{k}}^2=\mu_0^2[(1+\Delta)^2-\gamma_{\vec{k}}^2]\,, \tag{17}$$

where

$$\mu_0=SJ(0)=4SJ\,,$$

$$\gamma_{\vec{k}}=\tfrac{1}{4}\textstyle\sum_{\vec{n}} e^{i\vec{k}\cdot\vec{n}}=\tfrac{1}{2}(\cos k_x a+\cos k_y a)\,,$$

$$\Delta=H_A/4J\,.$$

Similarly, the Raman Hamiltonian is a simple modification of Eq. (3). With only nearest-neighbor intraplanar interactions,

$$H_{\text{Raman}}=\sum_{\vec{j},\vec{n}} B\left(\frac{\vec{E}_t\cdot\vec{E}_t'}{2}-\frac{(\vec{E}_t\cdot\vec{n})(\vec{E}_t'\cdot\vec{n})}{n^2}\right)\vec{S}_{\vec{j}}\cdot\vec{S}_{\vec{j}+\vec{n}}\,, \tag{18}$$

where the t subscripts refer to the transverse planar components. Additional polarization factors in Eq. (18) contribute only to the uniform Green's-function mode. These terms commute with the spin Hamiltonian and do not cause Raman scattering, so they have not been included. This interaction Hamiltonian is also the sum of uncoupled [2] Hamiltonians. Since the $S_{\vec{j}}^z S_{\vec{j}+\vec{n}}^z$ terms will have little effect on the scattering mode, as in the previous treatment we shall examine only the Green's functions arising from the transverse spin components.

All of the Green's-function equations for the ferrimagnetic case are valid for K_2NiF_4 with $S_a=S_b=1$, with the only minor changes coming from the number of nearest neighbors and the details of the symmetry transformations. The noninteracting Green's function is

$$G_{\vec{n}\vec{n}'}^a(E)=(-1)^{(p+q)/2+1}\frac{1}{(zSJ)^2}\left(\frac{S(p,q,\mathcal{E})+iC(p,q,\mathcal{E})}{\mathcal{E}}\right), \tag{19}$$

where

$$\mathcal{E}=[4(1+\Delta)^2-(E/zSJ)^2]^{1/2}\,,\quad \vec{n}-\vec{n}'=a(p,q)\,,$$

$$S(p,q,\mathcal{E})=\int_0^\infty \sin(\mathcal{E}t)J_p(t)J_q(t)\,dt\,,$$

$$C(p,q,\mathcal{E})=\int_0^\infty \cos(\mathcal{E}t)J_p(t)J_q(t)\,dt\,.$$

These integrals can be found from tabulated associated Legendre functions.[42,43] The symmetrized noninteracting scattering Green's function is $G_s^a=G_{00}^a+G_{20}^a-2G_{11}^a$. The scattering intensity is then proportional to

$$\mathrm{Im}G_s\propto \mathrm{Im}\left(\frac{[2zJS(1+\Delta)-J]G_s^a}{1+J[4zJS(1+\Delta)-J]G_s^a}\right)\,. \tag{20}$$

The theoretical Raman spectrum obtained from Eq. (20) with $\Delta=0$, $z=4$, and $S=1$ for the case of K_2NiF_4 is shown in Fig. 5 along with the predicted noninteracting spectrum. Note that there are no critical-point slope discontinuities as occur in the [3] Brillouin zone. The peak of the interacting magnon

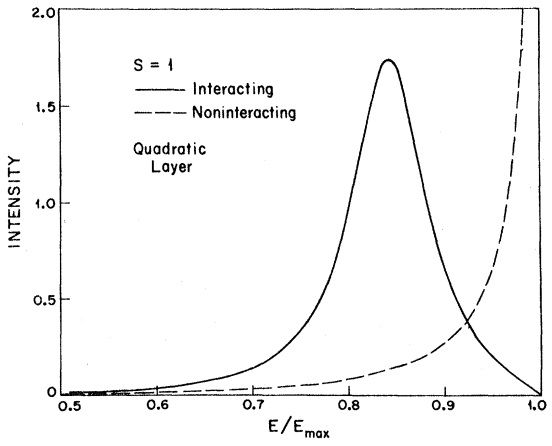

FIG. 5. Theoretical two-magnon Raman spectrum for K_2NiF_4 with $\Delta=0$, as a function of normalized energy.

spectrum is located at a normalized energy $E/E_{max} = 0.843$, compared with the Ising-model prediction $(2zS-1)/2zS = 0.875$. Our results for $S = \frac{5}{2}$ are identical with those shown in Fig. 5 of Ref. 41. In the crystal coordinate system the polarization factor from Eq. (18) gives the scattered intensity as

$$I_s \propto |B|^2[(E_x E_x')^2 + (E_y E_y')^2 - 2E_x E_x' E_y E_y'] \operatorname{Im} G_s . \quad (21)$$

The experimental Raman spectrum of K_2NiF_4 obtained at 5 °K with 5145-Å radiation is shown in Fig. 6. Along with the phonon lines, the broad two-magnon peak centered near 520 cm^{-1} was observed. This identification was made from the line's shape and position and its temperature dependence. Although the signal-to-noise ratio for this sample was not large enough to allow accurate quantitative measurement of the line position and width at higher temperatures, its qualitative behavior was observed. Up to approximately 100 °K, the Raman shift decreased very slightly, on the order of 50 cm^{-1}, with a slight decrease in amplitude and increase in linewidth. It was difficult to follow the peak position in this temperature range, or to note the precise temperature at which it disappeared, but by 150 °K no sign of the two-magnon line was observable.

With the relatively temperature-independent background spectrum subtracted, the portion of the low-temperature two-magnon spectrum is shown in Fig. 7, with the shaded area indicating the experimental noise. Superimposed on the enlarged experimental spectrum is the spectrum predicted from Eq. (20) with $\Delta = 0$, $z = 4$, $S = 1$, and $J = 77.0$ $cm^{-1} = 110.9$ °K. This last parameter, with an uncertainty of approximately ± 2 cm^{-1} or ± 3 °K, was found by fitting the peak of the theoretical curve to coincide with the experimental data, as in the case for $KNiF_3$. Allowing for the large amount of noise in the Raman spectrum, the line shapes and widths are seen to be in good agreement for the two curves.

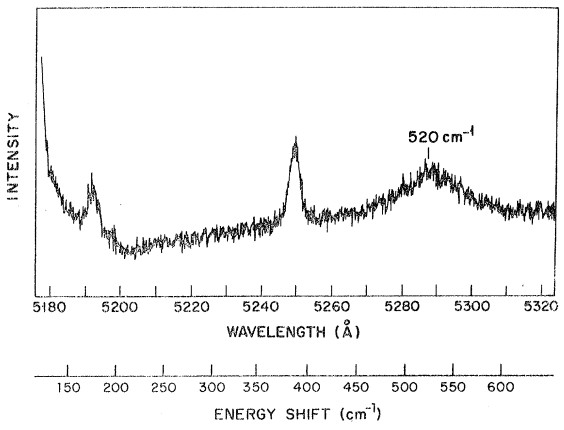

FIG. 6. Experimental Raman spectrum of K_2NiF_4 at 5 °K with 5145-Å excitation.

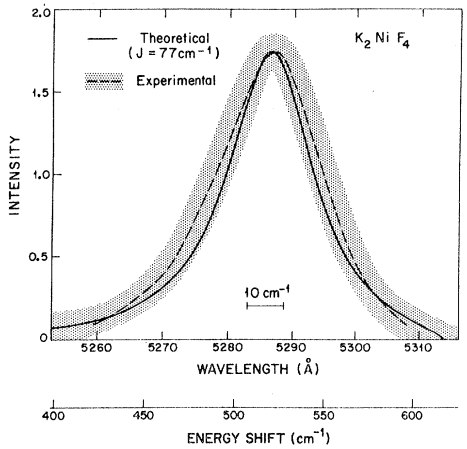

FIG. 7. Two-magnon portion of experimental Raman spectrum of K_2NiF_4 at 5 °K with theoretical spectrum calculated for $J = 77.0$ cm^{-1}. The shading indicates experimental noise.

Another interesting feature of the Raman-scattering experiment was strong dependence of the two-magnon scattering on the crystal orientation. As mentioned previously, it was much easier to transmit the laser beam along the direction of the crystal faults, and in this parallel configuration the 90° scattering showed a greatly improved Raman spectrum for the phonons, with almost a tenfold increase in signal, but with no visible two-magnon line. The spectrum with the two-magnon line shown in Fig. 6 was taken with the laser beam entering the sample perpendicular to the easy-transmission direction. This anisotropy is consistent with the picture of an anisotropic [2] scattering system, and might be explained from the preferential anisotropic orientation of the microcrystallites in the sample. If the radiation field vectors were perpendicular to the basal plane in the previously described parallel configuration, no spin-radiation scattering interaction would result, as given in Eq. (18).

V. STRUCTURE AND MAGNETIC PROPERTIES OF $RbNiF_3$

The normal-atmospheric-pressure phase of $RbNiF_3$ crystallizes in a hexagonal structure with space group D_{6h}^4,[44,45] and a configuration like that of the hexagonal modification of $BaTiO_3$.[46] A high-pressure phase of $RbNiF_3$[47] also exists which is a cubic perovskite antiferromagnet, similar to $KNiF_3$, but the present discussion will be limited to the hexagonal phase. This normal structure is ferromagnetic, with an ordering temperature T_c

= 139 °K.[48] Other experimental work in $RbNiF_3$ has been reported on such magnetic properties and behavior as magnetic resonance,[49] magnetization and susceptibility,[44,45,48,50] Faraday rotation,[51–53] and nuclear resonance.[53–55]

The structure of $RbNiF_3$ is shown in Fig. 8. There are six formula units per unit cell, both in the paramagnetic and ordered states, which results in a six-branched spin-wave spectrum. Each Ni^{2+} ion is located in an octahedron of six F^- ions, but these octahedra are not equivalent. Two-thirds of them have three F^- ions in common and share a face with each other, as well as sharing one F^- ion, or a corner, with the remaining one-third of the Ni^{2+}-F_6^- complexes. These different types of octahedra then contain different symmetry sites for the enclosed Ni^{2+} ions, labeled *B* (face shared) and *A* (corner shared).

As far as the magnetic properties of $RbNiF_3$ are concerned, the most important distinction between the two types of Ni^{2+} ions is that two adjacent *B* sites have approximately 90° Ni^{2+}-F^--Ni^{2+} superexchange interactions, while an *A*-*B* pair of sites has a 180° Ni^{2+}-F^--Ni^{2+} superexchange interaction. As in $KNiF_3$, this latter interaction is strongly antiferromagnetic, unlike the ferromagnetic *B*-*B* interaction, which does not exist in the cubic perovskite structure. The various factors contributing to these superexchange terms are described in the review article by Goodenough[56] and monograph by Anderson.[57] The two different signs of the exchange constants lead to a ferrimagnetic ground state, in which the *B* sites are parallel to each other and the *A* sites are antiparallel to them. Experimental measurement of the magnetic moment confirms that the net contribution to the saturation magnetization is one-third of the value expected if all spins were parallel.

In Fig. 8 the spin alignment has been shown along the *c* axis (for future reference) but $RbNiF_3$ actually has easy-plane anisotropy, with the lowest-energy spin orientations being in the basal plane perpendicular to the *c* axis. Measurements of the anisotropy field range from 23 to 30 kOe[44,45,48] for static fields and from 15 to 17 kOe[50] using pulsed-field techniques. However, the exact magnitude of the anisotropy field will not be too important in the present situation. Since we shall show that the anisotropy energy is so much smaller than the important exchange interactions, a good approximation will be to neglect the anisotropy altogether for the treatment of magnon energies. In this situation, any direction of spin alignment can be chosen.

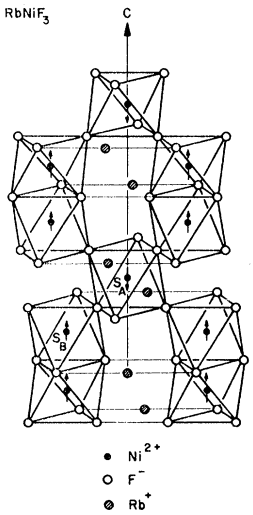

FIG. 8. Crystal structure of $RbNiF_3$.

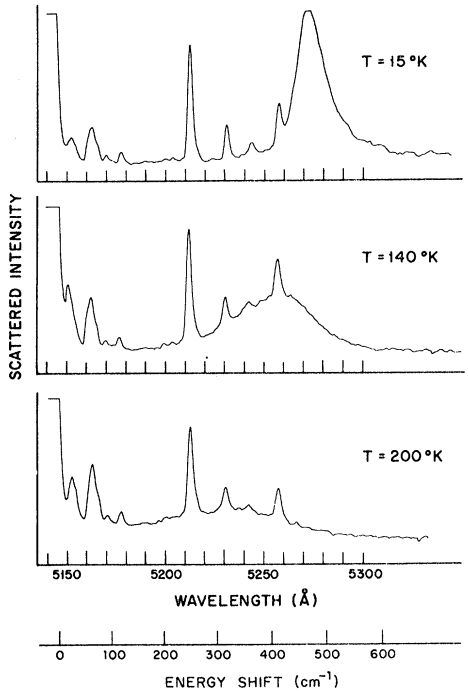

FIG. 9. Experimental Raman spectrum of $RbNiF_3$ with 5145-Å excitation at three temperatures, 15, 140, and 200 °K.

VI. EXPERIMENTAL RESULTS FOR $RbNiF_3$

The Raman spectrum of $RbNiF_3$ was measured using techniques similar to those described for $KNiF_3$ and K_2NiF_4. The major differences were in the wavelength analysis by a high-resolution double-grating spectrometer and the used of chopped excitation radiation with phase-sensitive synchronous detection of the scattered radiation. The final output signal, proportional to the intensity of the scattered radiation, was recorded on a strip-chart recorder as the spectrometer wavelength was swept. The spectra observed at three different temperatures are shown in Fig. 9, and are similar to those observed independently by Fleury *et al.*[11]

Apart from several narrow phonon lines whose positions did not shift noticeably with temperature, the most striking feature of the spectrum is the intense, broad line shifted at low temperature ~ 510 cm^{-1} from the excitation energy. Its Raman shift and linewidth as a function of temperature are shown in Fig. 10. Above 77 °K, the line broadened considerably and its Raman shift decreased. Evidence of it remained to temperatures over 200 °K ($1.4T_c$), well above the magnetic transition temperature, where it was shifted by approximately 320 cm^{-1} from the laser energy (19 450 cm^{-1} at a wavelength of 5145 Å). As in the case of $KNiF_3$, the maximum energy in the Raman spectrum of the line remained near its low-temperature value, about 570 cm^{-1}, but at the ordering temperature the line in $RbNiF_3$ was much better defined.

The best spectra (shown in Fig. 9) were obtained from an unoriented sample. Using an oriented crystal, suffering from cracks and inclusions, showed that the XZ and YZ components of the scattering tensor were largest (X, Y, and Z are the crystal coordinate axes with $Z \| c$ axis; the tensor indices refer to the incident and scattered light polarizations, respectively). It is not certain whether the scattered intensity in the other configurations, which was two to three times smaller, was due to crystal imperfections and misalignment. Such might be the case, since none of the phonon lines completely disappeared for the different scattering orientations, but extrapolating from the case of $KNiF_3$, it is also reasonable to expect both diagonal and off-diagonal scattering tensor elements. No change in the line shape of this broad line were observed for the different polarizations and beam orientations. Fleury *et al.*[11] found no visible changes in this Raman line in saturating magnetic fields of 50 kOe, applied both parallel and perpendicular to the crystal c axis.

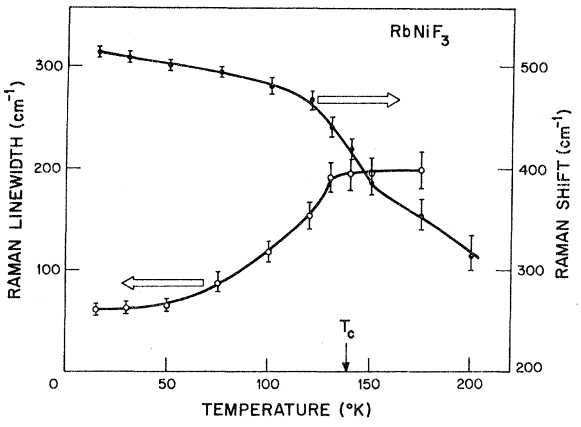

FIG. 10. Experimental peak position and width (full width at half-maximum) of the two-magnon Raman line in $RbNiF_3$ as a function of temperature.

This experimental evidence leads to the conclusion that the strong temperature-dependent Raman line in $RbNiF_3$ is caused by scattering from two magnons, as in an antiferromagnet. As analyzed below, the magnon branches in $RbNiF_3$ are more complicated than in a simple two-sublattice structure, but the same general features and restrictions for Raman scattering still apply. The dominant scattering interaction probably involves only terms in $\vec{S}_i \cdot \vec{S}_j$, with the additional assumption that sites i and j are on neighboring oppositely directed sublattices. This automatically precludes having both excitations on equivalent sublattices since the terms $S_i^+ S_j^+$ or $S_i^- S_j^-$ necessary to create the magnons in this case are not present. In a magnetic field, two magnons excited on the same type of sublattice would have their total energy shifted by approximately $2g\mu_B H$ (where μ_B is the Bohr magneton), while oppositely polarized magnons would each have opposite signs to their Zeeman shifts and give zero net energy difference. No effect of the magnetic field was observed by Fleury *et al.*,[11] supporting the fact that one magnon is primarily on the A (down) sublattice and the other associated with the B (up) sublattices. The fact that the intensity, position, and line shape of the Raman spectrum do not depend on the direction of spin alignment with respect to the crystal axes also supports the assignment of the form of the interaction $\vec{S}_A \cdot \vec{S}_B$ and shows the negligible effect of magnetic anisotropy on the scattering results. Other interaction mechanisms, such as the spin-orbit coupling, which do allow simultaneous excitation of two up or down spins can also cause second-order scattering, but these are generally smaller than the exchange-scattering mechanism, and in the present case are probably not important.

The other general feature which must apply for Raman scattering is that the two magnons have approximately equal and opposite wave vector, since the scattering wave vector for the radiation is essentially zero compared to wave vectors in the Brillouin zone. Since the magnon dispersion relations should flatten out near most of the Brillouin-zone edge, the density of states will be highest there, and we expect that the main contribution to the two-magnon Raman scattering will come from magnons near the zone edge. With this in mind, we shall next analyze the magnon spectrum of $RbNiF_3$ in detail. Because of the complex crystal structure of $RbNiF_3$, it is very difficult to apply the Green's-function technique directly to the two-magnon problem. Therefore, we shall first treat the problem on the basis of scattering from free magnons, and after finding the exchange constants, show that the Raman spectrum is at least consistent with their predictions and a simple flat-band estimate of the two-magnon interaction correction.

VII. ANALYSIS OF EXCHANGE CONSTANTS OF $RbNiF_3$

A. Spin-Wave Dispersion Relations

In analyzing the free magnon energies and interpreting the Raman spectrum, we take into account the following first-nearest-neighbor exchange parameters (see Fig. 11): (i) $J_{BB'}$ for nearest B neighbors in face-shared octahedra and (ii) J_{AB} for nearest A-B neighbors in corner-shared octahedra. In addition, we shall consider the much smaller second-neighbor interactions: (a) J_{BB} for hexagonal plane B-B second nearest neighbors, (b) J_{AA} for hexagonal plane A-A interactions, and (c) $\hat{J}_{BB}$ for second nearest B-B neighbors separated by an A plane. Since roughly the same type and number of Ni^{2+}-F^--F^--Ni^{2+} superexchange paths hold for these A-A and second-neighbor B-B interactions, we shall assume that $J_{AA} \simeq J_{BB} \simeq \hat{J}_{BB}$. For simplicity, we neglect other interactions, which we assume to act in most respects additively with, and to be much smaller than, the dominant J_{AB} and $J_{BB'}$ interactions. Some of these additional terms will be included in the theoretical analysis for generality, but we shall eventually set them equal to zero. The final values for these individual small interactions will probably not be too accurate, but since there are so many of them, their effect could be significant, and they should be included in an approximate way. In fact, early analysis[48] of susceptibility data by a molecular-field method showed an anomalously large intralattice A-A interaction, which, although inaccurate (as described later), does indicate the need to consider such parameters.

We begin by determining the magnon energies as a function of wave vector in terms of the unknown exchange constants. The method is essentially that used by Harris[58] for examining the magnon spectrum of yttrium and gadolinium iron garnet. Instead of finding the normal modes by use of second-quantized creation and annihilation operators, we shall obtain equations which are completely equivalent to the classical ones, by finding and solving the equations of motion for the spin raising and lowering operators, $S^+ = S^x + iS^y$ and $S^- = S^x - iS^y$. Initially, we shall neglect anisotropy and later we shall verify the validity of this assumption.

The spin-system Hamiltonian is

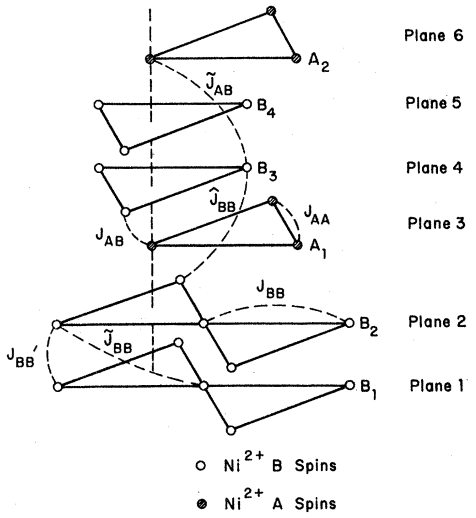

FIG. 11. Spin positions, labels, and exchange interactions in $RbNiF_3$.

$$\mathcal{H} = \sum_{jl} J_{jl}\, \vec{S}_j \cdot \vec{S}_l - g\mu_B \vec{H}_0 \cdot \sum_j \vec{S}_j \ , \tag{22}$$

where J_{jl} are the exchange constants described above and are shown with the site labels in Fig. 11. $\vec{H}_0$ is an applied magnetic field which is taken to be along the z axis, and the first summation is over distinct pairs. The Zeeman term here has a negative sign only for later convenience in identifying the mode polarizations. From the equation of motion for S_l^+, assuming a time variation $e^{i\omega t}$, and making the approximation of replacement of S^z by its average (or here, zero-temperature) value, we find

$$\omega S_l^+ = S_l^+ \left(\sum_j J_{lj} \langle S_j^z \rangle_0 - g\mu_B H_0\right) - \langle S_l^z \rangle_0 \sum_j J_{lj} S_j^+ \ . \tag{23}$$

A similar equation exists for S_l^-, and for either type of operator there will be six such equations, one for each of the six sublattices. Since the raising and lowering operators are uncoupled, we need solve for only one of them and we choose to solve Eq. (23). After making the Fourier decomposition $S_\Gamma^{j+} \sim S_\Gamma^+ e^{i\vec{k}\cdot\vec{r}_j}$ (where Γ labels the sublattice and j the site) and taking $\langle S_B^z \rangle_0 = +1$ and $\langle S_A^z \rangle_0 = -1$, we obtain six equations, summarized in the following matrix equation:

$$\begin{array}{c|cccccc}
 & S_{B_1}^+ & S_{B_2}^+ & S_{B_3}^+ & S_{B_4}^+ & S_{A_1}^+ & S_{A_2}^+ \\
\hline
S_{B_1}^+ & \mathcal{J} & -J_{BB'} - \tilde{J}_{BB}\eta & 0 & -\hat{J}_{BB} e^{ik_z c}\xi' & -\tilde{J}_{AB}\xi & -J_{AB} e^{ik_z c}\xi \\
S_{B_2}^+ & -J_{BB'} - \tilde{J}\eta & \mathcal{J} & -\hat{J}_{BB}\xi' & 0 & -J_{AB}\xi & -\tilde{J}_{AB} e^{ik_z c}\xi \\
S_{B_3}^+ & 0 & -J_{BB}\xi'^* & \mathcal{J} & -J_{BB'} - \tilde{J}_{BB}\eta & -J_{AB}\xi & -\tilde{J}_{AB}\zeta \\
S_{B_4}^+ & -\hat{J}_{BB} e^{-ik_z c}\xi'^* & 0 & -J_{BB'} - \tilde{J}_{BB}\eta & \mathcal{J} & -\tilde{J}_{AB}\zeta & -J_{AB}\zeta \\
S_{A_1}^+ & \tilde{J}_{AB}\xi^* & J_{AB}\xi^* & J_{AB}\zeta^* & \tilde{J}_{AB}\zeta^* & \mathcal{J}' & 0 \\
S_{A_2}^+ & J_{AB} e^{-ik_z c}\xi^* & J_{AB} e^{-ik_z c}\xi^* & \tilde{J}_{AB}\zeta^* & J_{AB}\zeta^* & 0 & \mathcal{J}'
\end{array} = \omega \underline{1}_{6\times 6} = \underline{A} \ . \tag{24}$$

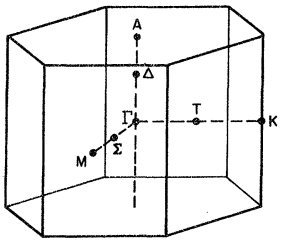

FIG. 12. Brillouin zone for hexagonal $RbNiF_3$.

The row and column labels are shown, and the factors in the matrix are

$$\mathcal{J} = J_{BB}(6-\eta) + J_{BB'} + 6\tilde{J}_{BB} + 3\hat{J}_{BB} - 3J_{AB} - 3\tilde{J}_{AB} - g\mu_B H_0,$$

$$\mathcal{J}' = -J_{AA}(6-\eta) + 6J_{AB} + 6\tilde{J}_{AB} - g\mu_B H_0,$$

$$\zeta = 1 + 2\cos\tfrac{1}{2}k_x a\, e^{ik_y\sqrt{3}\,a/2},$$

$$\eta = 2\cos k_x a + 4\cos\tfrac{1}{2}k_x a\cos k_y \tfrac{1}{2}\sqrt{3}\,a/2,$$

$$\xi = 1 + e^{ik_x a} + e^{1/2i(k_x a + k_y\sqrt{3}a)},$$

$$\xi' = 1 + e^{ik_x a} + e^{1/2i(k_x a - k_y\sqrt{3}\,a)}.$$

For completeness we have included the extra interactions $\tilde{J}_{BB}$ and $\tilde{J}_{AB}$, although they have slightly different types of superexchange paths than considered before, and will later be dropped. The hexagonal layer spin spacing is a and the z-axis unit-cell length is c. A star (*) denotes complex conjugation. The matrix in Eq. (24) is not Hermitian, but its roots must be real if the assumed ground state is stable with respect to dynamic spin fluctuations. The mode energies are found by taking the magnitudes of the (real) frequencies found from the solution of Eq. (24).

For certain directions in the Brillouin zone, shown in Fig. 12, analytic solutions of Eq. (24) can be found, which relate the magnon energies to the exchange constants. The solutions of this equation for various directions in the Brillouin zone are shown in Fig. 13. Analytic expressions for the energies at $\vec{k} = \Gamma$ and K are shown and the schematic representation of the amplitudes and phases of S_i^+ are pictured in Figs. 14 and 15. The numerical values of the exchange constants used in these calculations are given in Sec. VIII.

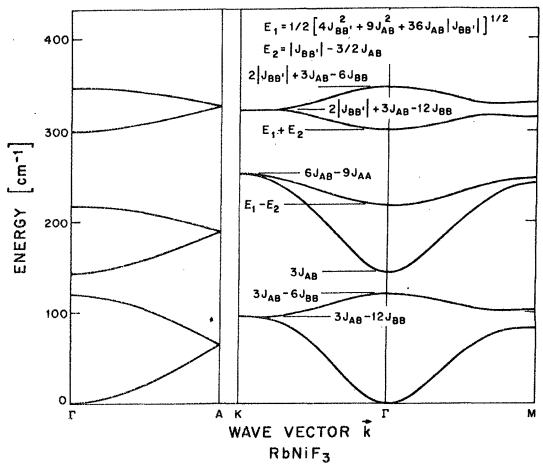

FIG. 13. Magnon dispersion relations in $RbNiF_3$.

In Fig. 14, the modes which correspond to those Γ point energies shown in Fig. 13 are, in increasing order from zero energy, U_1, U_3, U_2, U_6, U_5, and U_4. The U_1 mode at zero energy and the U_2 mode with energy $3J_{AB}$ have uniform symmetry and could be Raman active for one-magnon scattering. However, unless the scattering matrix elements differ for A and B sites, the U_2 mode will not be observable because the sum of the transverse spin moments for all six sites is zero.

In Fig. 15, the doubly degenerate K-point modes in order of increasing energy are $U_1 + U_3$, $U_2 + U_6$, and $U_4 + U_5$. We observe two-magnon Raman scattering from the combinations similar to $U_2 + U_6$ and $U_4 + U_5$, although the $U_2 + U_6$ and $U_1 + U_3$ combinations would also seem to be allowed.

This analysis assumed an arbitrary direction for the alignment of the net moment of S^z axis, arbitrarily taken to be along the crystal c axis. The actual ground-state configuration is with the spins lying in the xy plane of the crystal, perpendicular to the c axis. Choosing a direction in the basal plane for the S^z axis, and applying a small negative anisotropy field perpendicular to the basal plane, the same type of calculation was carried out as before. However, in this situation the S^+ and S^- modes are mixed by the anisotropy field and the equations of motion have to be found for the Car-

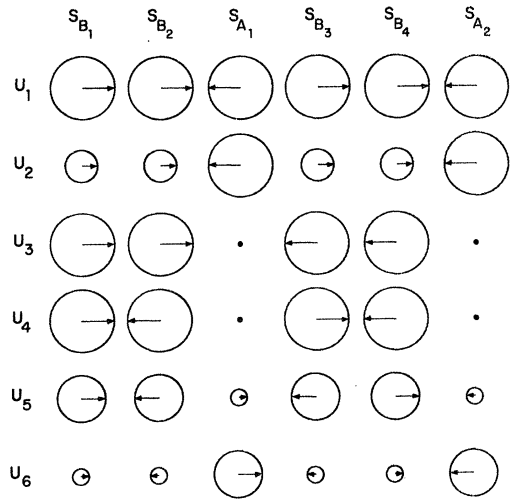

FIG. 14. Schematic representation of amplitudes and phases for $S_{A_i}^+$ and $S_{B_i}^+$ at $\vec{k} = \Gamma$.

tesian spin components. This results in a set of 12 equations, leading to a 12×12 matrix. Diagonalization of this matrix using the numerical exchange constants and an anisotropy parameter obtained from an anisotropy field of 20 kOe gave results for the magnon energies unchanged to within the anisotropy energy, ~3 °K. Since the Raman scattering is unaffected by external magnetic fields capable of changing the spin orientation, and since the numerical results show no large effects of anisotropy, the original plus- and minus-mode description was retained throughout the following analysis.

The normal-mode solutions given above were first found by inspection, and later obtained in a simple manner by means of group-theoretical methods. These latter methods are of interest, because they show explicitly the structure and degree of complexity of the equations of motion for other directions and points in the Brillouin zone. The analysis uses the spin space-group method of Brinkman and Elliott,[59,60] since we have assumed the Heisenberg Hamiltonian to which the theory applies. Inclusion of the spin-orbit or dipolar interactions would necessitate the use of the full magnetic space group.

For a general $\vec{k}$ in the Brillouin zone, the full 6×6 matrix of Eq. (24) must be diagonalized, but for $\vec{k}$ along certain symmetrical directions, the equations may be simplified. With the aid of the compatibility relations,[61] we are able to find the symmetry representations along the Δ, T, and Σ directions. This points out the particularly simple nature of the solutions along T, because the representations T_3 and T_4 occur once and T_1 and T_2 occur only twice, leading to two first-order and two quadratic secular equations, while for both the Δ and Σ directions two cubic equations result.

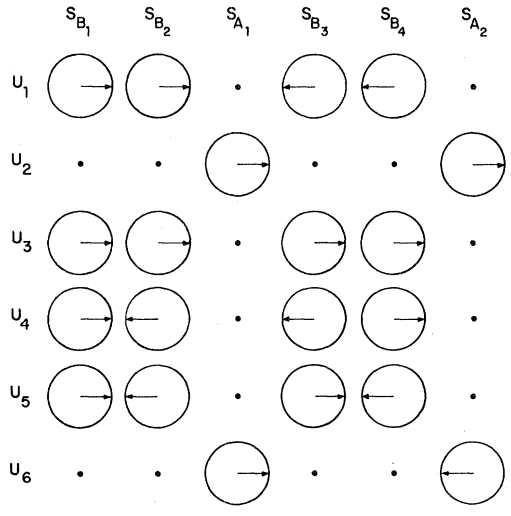

FIG. 15. Schematic representation of amplitudes and phases for $S^{+}_{A_i}$ and $S^{+}_{B_i}$ at $\vec{k}=K$.

Because of the particularly simple nature of the equations for a wave vector along T, we are able to find a simple explicit expression for the uniform-mode energy at small wave vector. For $ka\ll1$, the lowest spin-wave energy is given by

$$E=D(ak)^2, \tag{25}$$

where D is the exchange stiffness constant. From the solution of the secular equations along T we obtain

$$E=(J_{AB}+\tilde{J}_{AB}-\tfrac{3}{2}J_{AA}-3J_{BB}-3\tilde{J}_{BB}-\tfrac{1}{2}\hat{J}_{BB})(ak)^2. \tag{26}$$

This result is physically reasonable, since it shows that the energy is dominated by the large antiferromagnetic exchange J_{AB}. The ferromagnetic coupling $J_{BB'}$ does not appear because the B spins precess in phase; the small antiferromagnetic terms which compete with J_{AB} tend to make the Néel configuration unstable and lower the acoustic-mode energy. It should be remembered that anisotropy, which would lead to an additional energy gap at small $\vec{k}$, has been neglected.

B. Interpretation of a Magnon-Sideband-Absorption Experiment

Several workers have measured the optical-absorption spectrum in $RbNiF_3$.[62–65] In particular, Zanmarchi and Bongers[64] measured the absorption spectrum in the visible and infrared with emphasis on the $^3A_2\rightarrow{}^1E$ transition near 15 000 cm^{-1}. At low temperature they observed four closely spaced lines, two of which disappeared as the Curie temperature was reached. As the temperature was raised the separation of each of these two lines from its partner in the remaining pair was reduced. Their conclusions were that the two main peaks were absorptions from the $^3A_2\rightarrow{}^1E$ vibronic transitions of the Ni^{2+} ions, and were separated because of the different crystal-field environment of the A and B sites. The additional two absorption lines were then interpreted as being magnon sidebands to these transitions. The low-temperature energy separation of the sideband to the A-site transition was about 320 cm^{-1}, and the B-site magnon sideband energy was approximately 250 cm^{-1}. We will make the physically reasonable assumption that the A-site sideband is due to absorption at an A site, accompanied by the creation of a magnon on the B sublattice; and the B-site sideband is due to the creation of a magnon on the A sublattice.

Using the previous analysis of the magnon dispersion relations, we assign the higher-energy B lattice magnon associated with an A-site absorption the energy 320 cm^{-1}. Similarly, the A lattice

magnon has an energy 250 cm^{-1}. We assume that the high-density-of-states zone-edge magnons are the most important in the scattering and absorption. For simplicity, we use the analytic expressions for the magnon energies found at the K point, a good approximation since the transversely directed magnons have approximately the same zone-edge energies, and those in the z direction with slightly different energies have a much lower density of states.

With this assignment, we have the following two relations at the K point:

$$E_{4,5} = E_B = 2|J_{BB'}| + 3J_{AB} - 9J_{BB} - 3\hat{J}_{BB'} \simeq 320\ \mathrm{cm}^{-1}$$

and (27)

$$E_{2,6} = E_A = 6J_{AB} - 9J_{AA} \simeq 250\ \mathrm{cm}^{-1}.$$

The exchange constant $\tilde{J}_{AB}$ has been included in J_{AB}, and $\tilde{J}_{BB}$ has been neglected, to conform with the previous discussion and labeling of the exchange constants. Since we have included the second-neighbor interactions (to be set equal to each other), we need an additional relation to determine uniquely the three unknown J's. This is obtained from a molecular-field analysis of the susceptibility data for $RbNiF_3$.[45,48] We use the high-temperature value of $\chi^{-1}(T)$ to estimate the paramagnetic Curie temperature (or negative temperature intercept) θ_c. From a molecular-field analysis we find that

$$k|\theta_c| = \tfrac{2}{9}(6J_{AA} + 12J_{BB} + 6\tilde{J}_{BB} + 12J_{AB} + 2J_{BB'}). \quad (28)$$

The molecular-field method is quite unreliable near T_c, but we expect that the high-temperature results are better. The value given for θ_c in Ref. 45 is $-130\,^\circ$K, while Ref. 48 quotes $-330\,^\circ$K. We estimate that $k|\theta_c| \simeq 100\ \mathrm{cm}^{-1} \simeq 144\,^\circ$K, which we feel is a better asymptote to the susceptibility data drawn in Ref. 48 and more in agreement with the first value quoted. Setting all the second-neighbor interactions equal, Eqs. (27) and (28) are solved to give

$$\begin{aligned} J_{AB} &= 48 \pm 3\ \mathrm{cm}^{-1}, \\ J_{BB'} &= -113 \pm 3\ \mathrm{cm}^{-1}, \\ J_{AA} \simeq J_{BB} \simeq \hat{J}_{BB} &= 4 \pm 4\ \mathrm{cm}^{-1}. \end{aligned} \quad (29)$$

Figure 13 shows the magnon dispersion relations obtained by solving Eq. (24) for various directions of wave vector, computed using these numerical values. The approximate errors which we quote arise from the uncertainty in θ_c. As expected, the second-neighbor interactions are more sensitive to errors in θ_c, but these are intended to be only rough correction factors, accurate to within a factor of 2 or so.

At this point we return to the description of the two-magnon Raman excitation, which was the motivation for analyzing the spin-wave spectrum and exchange constants in such detail. In finding these parameters we have not used any data from the Raman-scattering measurements, and we now examine the scattering results using the information about the spin-wave energies.

The approximation to the magnon-interaction effects which we shall use is the Ising or flat-band model, which was discussed by Elliott and Thorpe[3] and in Sec. II. This model uses an Ising-spin Hamiltonian with only S^zS^z interaction terms, and for the simple antiferromagnets yields a good semiquantitative estimate of the location of the Raman spectral peak. Even though the actual spin interactions are very nearly isotropic, this simple anisotropic model works well because its δ-function joint density of states resulting from a flat magnon dispersion relation closely resembles the narrow sharply peaked joint density of states found from the Heisenberg model. Thus the simplest estimate of the binding, as found from the Ising flat-band model, is a subtraction of the exchange energy of the excited spin pair from the "noninteracting" two-magnon energy. As shown in Sec. II, the presence of a net moment in the ferrimagnetic ground state and an optical branch of the magnon spectrum does not cause any major qualitative differences in the two-magnon spectrum from the simple antiferromagnet.

We see that the most plausible assignment for the Raman line is the combination of two zone-boundary magnons with opposite wave vectors, one on the A sublattice with energy approximately 250 cm^{-1} and the other on the B sublattice with energy about 320 cm^{-1}. Both of these bands are rather narrow and flat, and their joint density of states should peak sharply near the zone-edge energy, in the transverse directions leading to this emphasis of transverse boundary magnons and to the use of the flat-band approximation to estimate the binding correction. The sum of these two energies is 570 cm^{-1}, about 60 cm^{-1} greater than the observed location of the Raman peak. However, using the flat-band approximation, we can estimate the magnon-magnon interaction effects by subtracting the energy J_{AB} from the expected noninteracting peak energy to allow for the proximity of the simultaneous A and B spin excitations. This gives a predicted location of $570 - 48 = 522$ cm^{-1} for the Raman line, in good agreement with the experimental value, 510 cm^{-1}. In fact, a more rigorous computation of the interaction with a Heisenberg model would probably give yet a larger correction.

A further point which we have examined is the dynamic stability of the Néel configuration. This method, used by Kaplan[66] for the cubic spinel structure, is based on an expansion of the Heisenberg

exchange energy to second order in the deviations of the spins from the Néel state. While it is formally necessary to solve the resulting eigenvalue equation throughout the Brillouin zone, we feel that the most stringent stability criterion is met for transverse $\vec{k}$ vectors. This analysis for the Σ direction yields

$$J_{AB}+\tilde{J}_{AB}-\tfrac{3}{2}J_{AA}-3J_{BB}-3\tilde{J}_{BB}-\tfrac{3}{2}\hat{J}_{BB}>0 \qquad (30)$$

for local stability. This stability criterion is more stringent than that obtained from a molecular-field calculation. It is satisfied by the parameters (29), but is not satisfied by exchange constants obtained from molecular-field parameters of Ref. 48.

VIII. PREDICTION OF MAGNETIC PROPERTIES FOR $RbNiF_3$ FROM EXCHANGE PARAMETERS

A. Introduction

In this section we shall examine the predictions of several theories as applied to $RbNiF_3$ in an attempt to provide additional verification of the previously derived exchange constants. By comparing the theoretical and measured values of such quantities as the Curie temperature and sublattice magnetizations, we hope to show that the exchange constants consistent with the optical-absorption and Raman-scattering measurements are indeed realistic estimates for $RbNiF_3$.

In principle, knowing the spin interactions, we can calculate the macroscopic magnetic properties to any required degree of accuracy, but in practice the computational difficulties force us to choose some sort of approximate scheme for doing so. The properties which we hope to derive are highly dependent on the approximations which are made or on the model which is chosen. Therefore, we must exercise some care in choosing a method which is not prohibitively difficult to examine, but which does have a high degree of accuracy.

The molecular-field (MF) model, the simplest and perhaps most widely used, gives qualitatively correct results for magnetic properties such as magnetization and ordering temperature, but its neglect of short-range order can cause large quantitative errors. For example, these discrepancies can be as large as 50% in evaluation of the Curie temperature for low values of spin and number of nearest-neighbor interactions. The Oguchi method, a modification of the MF method, treats an exchange-coupled pair of spins in a molecular field, but still retains most of the MF method's limitations. High-temperature expansion methods are considered quite accurate if a sufficient number of terms in the expansion are used; however, they are numerically involved, and would be quite difficult in the case of $RbNiF_3$ with its two different dominant exchange interactions and its relatively complicated lattice. The BPW method, which we shall examine in detail, is a cluster calculation which explicitly considers the interactions among a small number of spins, and then treats this cluster in a molecular-field type of calculation. A good review of the molecular-field and cluster methods is found in the monograph by Smart.[67]

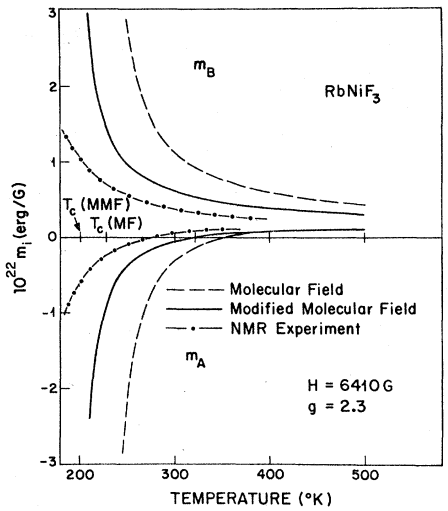

FIG. 16. Sublattice magnetizations in $RbNiF_3$ above T_c as a function of temperature as found from molecular-field and modified molecular-field calculations and NMR experiments.

Along with the ordering temperature, further experimental measurements with which to compare the theoretical results in $RbNiF_3$ are the sublattice magnetizations as a function of temperature. Smolenskii *et al.*[53–55] have performed NMR measurements on the F^{19} nuclei located at the two different types of sites in $RbNiF_3$. Over the temperature range 150–400 °K they measured the resonance frequencies of the F^{19} nuclei, and obtained the variation of the individual sublattice magnetizations as a function of temperature in the applied external field. Their results are shown in Fig. 16. A striking feature of their findings is that over a wide temperature range above the ordering temperature the A sublattice magnetization is antiparallel to the applied field. This result, which is surprising at first glance, can be understood from the qualitative features of the exchange parameters which we have derived. As expected, the B lattice moments line up parallel with the field. The magnetic field torque on the A lattice is only half as great since there are twice as many B sites, and the most important factor in determining the direction of the magnetic moments m_A is the large antiferromagnet exchange J_{AB}. This exchange is strong enough so that even for $T>T_c$ the short-range correlations remain and make the lattices antiparallel in the applied field. As the temperature is increased

and the thermal excitation and applied field torque overcome the exchange forces, m_A reverses sign and both sublattice magnetizations become parallel to the field. The experimental measurements give this temperature to be $T_0 = 280\ ^\circ\mathrm{K}$.

B. Quantum-Mechanical BPW Method

Molecular-field and modified Oguchi-type molecular-field calculations have been carried out[10] and the results are shown in Fig. 16. The neglect of short-range order leads to the poor agreement with experiment. Because of this deficiency in the theory we have used the BPW method to calculate T_c, T_0, and $m_{A,B}$.

The BPW method is a type of molecular-field treatment which considers a cluster of spins, the central spin having exchange interactions with its surrounding spins, and those outer spins being acted on by an effective molecular field from the rest of the magnetic system. This model differs from simpler molecular-field models in that at least one of the spins under consideration is not in a molecular field, and the effective field on the outer cluster spins is not assumed to be proportional to a sublattice magnetization. This method is quite similar to the constant-coupling model[68, 69] which uses an effective spin-pair Hamiltonian.

The BPW method is chosen for the quantitative examination of the magnetic behavior of $RbNiF_3$ for several reasons. (i) It gives better results for ordering temperatures than either the molecular-field or Oguchi methods, without an unmanageable increase in difficulty. (ii) Its accuracy compares favorably with the more exact high-temperature expansion method, which would be prohibitively difficult to apply to the structure of $RbNiF_3$, particularly if second-nearest-neighbor interactions are included. (iii) The BPW high-temperature results are extremely close to those of the constant-coupling model which, although having better low-temperature properties, cannot be extended to $RbNiF_3$ in so straightforward a manner as the BPW method.

The basic ideas of the BPW method are quite simple. First, a cluster of spins is chosen, whose outer spins are acted on by effective molecular fields, and then the cluster partition function is found. From this, the different magnetizations are obtained in terms of the applied and as yet undetermined molecular fields. If different spin magnitudes or site symmetries are present in the cluster, more than one type of cluster must be examined. Finally, consistency relations which give the molecular fields and magnetizations are found by equating all equivalent magnetizations. In order to find the ordering temperature, the applied field is set equal to zero, and the temperature at which the molecular fields do not vanish is found.

Although this program is quite simple in principle, for the case of $RbNiF_3$ the actual calculations are tedious and complicated. The simplest method of calculation follows quite closely that of Brown and Luttinger.[70] First we shall state the quantum-mechanical problem and next examine a semiclassical approximation in more detail. In both cases the treatments are similar, and follow a perturbation or expansion scheme.

A brief summary of the steps of the first, quantum-mechanical, calculation for one cluster is as follows:

(a) Write the Hamiltonian of the cluster, separated into exchange and Zeeman terms.

(b) Find the exact eigenvalues of the exchange Hamiltonian.

(c) From perturbation theory find the cluster partition function to second order in the applied and molecular fields.

(d) Find all the magnetizations from the partition function.

This is done for both the A- and B-centered clusters. Then the magnetizations of all A-site Ni^{2+} ions are set equal, as are the magnetizations for all the B sites. In this calculation we neglect the second-neighbor interactions. They are included in the classical BPW calculation.

The first cluster consists of two central B spins surrounded by six A spins. (In the discussion of the BPW method, we write exchange constants as "$2J$" to conform to the notation of Ref. 70. Note that the exchange constants J_{AB}, $J_{BB'}$, etc., in previous sections do not appear with the factor 2.) Its Hamiltonian is

$$\begin{aligned}
&\mathcal{H}_B = \mathcal{H}_0 + \mathcal{H}_1 ,\\
&\mathcal{H}_0 = -2J\vec{S}_{B_1}\cdot(\vec{S}_{A_1}+\vec{S}_{A_2}+\vec{S}_{A_3}) \\
&\qquad -2J\vec{S}_{B_2}\cdot(\vec{S}_{A_4}+\vec{S}_{A_5}+\vec{S}_{A_6}) - 2\hat{J}\vec{S}_{B_1}\cdot\vec{S}_{B_2} ,\\
&\mathcal{H}_1 = -g\mu_B H_0(S^z_{B_1}+S^z_{B_2}) - g\mu_B H_1^B(S^z_{A_1}+\cdots+S^z_{A_6}) .
\end{aligned} \tag{31}$$

The eigenstates of $\mathcal{H}_0$ are given by $|\alpha\rangle$, with $\mathcal{H}_0|\alpha\rangle = E^0(\alpha)|\alpha\rangle$. All of these zero-field eigenstates and eigenvalues are found by numerical computation, for a given ratio of $\hat{J}/J$. Then, from second-order perturbation theory, the partition function is

$$Z_B = \sum_\alpha \exp[\tilde{E}^0(\alpha)]\left(1+\langle\alpha|\tilde{\mathcal{H}}_1|\alpha\rangle + \sum_{\alpha';\alpha'\neq\alpha}\frac{|\langle\alpha|\tilde{\mathcal{H}}_1|\alpha'\rangle|^2}{\tilde{E}^0(\alpha)-\tilde{E}^0(\alpha')} + \frac{|\langle\alpha|\tilde{\mathcal{H}}_1|\alpha\rangle|^2}{2}\right), \tag{32}$$

where the tilde denotes multiplication by $-1/kT$, i.e., $\tilde{E} = -E/kT$. This function is evaluated and the magnetizations are found from

$$m_B = \frac{g\mu_B}{2}\frac{\partial \ln Z_B}{\partial \lambda_0} , \quad m_A = \frac{g\mu_B}{6}\frac{\partial \ln Z_B}{\partial \lambda_1^B} ,$$

where

$$\lambda_0 = g\mu_B H_0/kT\,, \quad \lambda_1^B = g\mu_B H_1^B/kT\,. \tag{33}$$

The partition function Z_B has terms up to second order in the effective fields. The A-centered cluster is treated in a similar manner. After differentiating the partition functions to find the magnetizations, and constraining the A magnetizations found from the two clusters to be the same (and similarly for the B magnetizations), we find two linear equations in the unknown field parameters. Their coefficients are functions of J/kT and, implicitly, $\tilde{J}/J$. To find the ordering temperature we set $\lambda_0 = 0$ and find where the effective fields λ_1^A and λ_1^B do not vanish. This occurs when the determinant resulting from the linear equations equals zero.

Using the experimentally determined ratio $\tilde{J}/J = -2.36$, the numerical solution gives $kT_c/|J| = 4.74$, or in terms of the original notation, $kT_c/J_{AB} = 2.37$. With the value $J_{AB} = 48\ \mathrm{cm}^{-1} = 69\ ^\circ\mathrm{K}$, the computed ordering temperature is $T_c = 163\ ^\circ\mathrm{K}$, a significant improvement over the molecular-field results. Next, we shall make some approximations in a more extensive BPW calculation including second-neighbor exchange and show that not only the predicted ordering temperature, but sublattice magnetizations as well, are quite close to experimental values.

C. Classical BPW Method

The preceding result of the final quantum-mechanical calculation for T_c, 163 °K, is about 17% higher than the actual measured value, 139 °K. If the experimental exchange constants are correct, this is not an unreasonable error for such a calculation, particularly since the second-neighbor interactions, which were not included, tend to lower the ordering temperature. Since the classical BPW method is a good approximation to the quantum-mechanical version and is much easier to work with, we have made a final classical BPW calculation for $RbNiF_3$ in which are included not only the dominant J_{AB} and $J_{BB'}$ interactions, but second-nearest-neighbor interactions as well.

The classical approximation to the BPW method has been examined by Brown and Luttinger[70] and Brown.[71] It generally gives excellent agreement with the quantum-mechanical BPW calculation (particularly for larger values of S and coordination number), and its greater simplicity often allows its application to more complex spin structures. The only difference between the classical method and the quantum-mechanical method as outlined above lies in the calculation of the partition functions. In the classical case, the spins are treated as classical vector quantities, their commutation properties are ignored, and the summation over quantum states is replaced by integration over the continuum of spin orientations. One feature retained from quantum mechanics is the final replacement of the spin magnitude S by the value $[S(S+1)]^{1/2}$. This is the same replacement which makes the classical Langevin function almost identical to the exact quantum-mechanical Brillouin function in the usual molecular-field problem.

The main difficulty in this extension lies in the inclusion of the additional further-neighbor interactions. A basic requirement of the simple BPW method is that spins in the outer cluster are not nearest neighbors of each other, ruling out the application to such lattices as the hexagonal layer and face-centered cubic. In $RbNiF_3$ this is no problem if only the two main interactions are considered, but when more distant neighbors are added to the cluster, they can have strong interactions among themselves. Brown[71] has demonstrated a method which accounts for interactions within the cluster by dividing the cluster shell spins into subshells such that spins within a subshell have no exchange interactions among themselves. After this division different molecular fields are allowed to act on each subshell. Such a treatment does lead to differences between ferromagnetic and antiferromagnetic lattices in the classical limit. However, it also gives the incorrect result that for the ferromagnetic hexagonal layer and face-centered-cubic lattices the intrashell interactions have no effect, as seen from symmetry considerations which require that molecular fields on equivalent cluster sites be equal. Nevertheless, this method is probably a good approximation for $RbNiF_3$ because of the weak nature of most interactions among the shell spins. If two shell spins do have a strong interaction between them, then at least one, and sometimes both, are coupled weakly to the central spins.

Using the symmetry of the assumed Néel configuration, the B-centered cluster is divided into

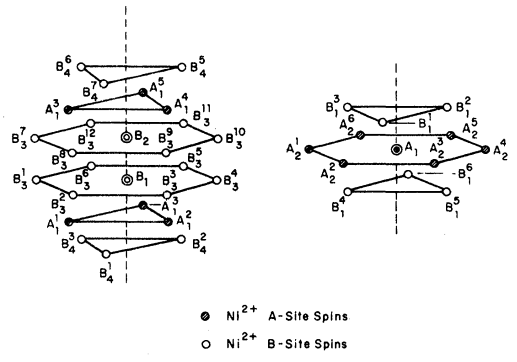

FIG. 17. Spin clusters used in the classical BPW calculation for $RbNiF_3$.

the central B spins and the shell of one A sublattice and two inequivalent B sublattices. These are shown and labeled in Fig. 17. The cluster Hamiltonian is

$$\begin{aligned}\mathcal{H}_B = &-2J\vec{S}_{B_1}\cdot[\vec{S}(A_1^1)+\vec{S}(A_1^2)+\vec{S}(A_1^3)]-2J\vec{S}_{B_2}\cdot[\vec{S}(A_1^4)+\vec{S}(A_1^5)+\vec{S}(A_1^6)]-g\mu_B\vec{H}_1^B\cdot[\vec{S}(A_1^1)+\cdots+\vec{S}(A_1^6)]\\ &-2\tilde{J}\vec{S}_{B_1}\cdot[\vec{S}(B_3^1)+\cdots+\vec{S}(B_3^6)]-2\tilde{J}\vec{S}_{B_2}\cdot[\vec{S}(B_3^7)+\cdots+\vec{S}(B_3^{12})]-g\mu_B\vec{H}_2^B\cdot[\vec{S}(B_3^1)+\cdots+\vec{S}(B_3^{12})]\\ &-2\tilde{J}\vec{S}_{B_1}\cdot[\vec{S}(B_4^1)+\vec{S}(B_4^2)+\vec{S}(B_4^3)]-2\tilde{J}\vec{S}_{B_2}\cdot[\vec{S}(B_4^4)+\vec{S}(B_4^5)+\vec{S}(B_4^6)]-g\mu_B\vec{H}_3^B\cdot[\vec{S}(B_4^1)+\cdots+\vec{S}(B_4^6)]\\ &-g\mu_B\vec{H}_0\cdot(\vec{S}_{B_1}+\vec{S}_{B_2})-2\hat{J}\vec{S}_{B_1}\cdot\vec{S}_{B_2}\,. \qquad (34)\end{aligned}$$

We have included only the interactions previously used in calculating the spin-wave energies with slight changes in notation. For simplicity all of the g factors are assumed to be equal, and the applied and molecular fields are parallel.

In the classical approximation, the partition function for the B cluster is

$$Z_B = \int d\Omega\, e^{-\mathcal{H}_B/kT}\,, \qquad (35)$$

where $\int d\Omega$ indicates integration over all spin orientations. The quantum-mechanical perturbation calculation is replaced by an expansion of the exponential Zeeman terms. The angular integrations are straightforward but tedious, and the final result to second order in the field parameters is

$$\begin{aligned}Z_B = (\text{const})\,[&1+\lambda_1^{B\,2}S_A^2(1+2L^2+3L^2\hat{L})+\lambda_2^{B\,2}S_B^2\\ &\times 2(1+5\tilde{L}^2+6\tilde{L}^2\hat{L})+\lambda_3^{B\,2}S_B^2(1+2\tilde{L}^2+3\tilde{L}^2\hat{L})+6(1+\hat{L})\\ &\times(2\lambda_1^B\lambda_2^B S_A S_B L\tilde{L}+\lambda_1^B\lambda_3^B S_A S_B L\tilde{L}+2\lambda_2^B\lambda_3^B S_B^2\tilde{L}^2)\\ &+2(1+\hat{L})\,\lambda_0(\lambda_1^B S_A S_B L+2\lambda_2^B S_B^2\tilde{L}+\lambda_3^B S_B^2\tilde{L})\\ &+\tfrac{2}{3}(1+\hat{L})\,\tfrac{1}{2}(\lambda_0^2 S_B^2)]\,, \qquad (36)\end{aligned}$$

where

$$\begin{aligned}&S_A=S_B=S, \qquad p=J/kT, \qquad \hat{p}=\hat{J}/kT,\\ &\tilde{p}=\tilde{J}/kT, \qquad \lambda_i^B=g\mu_B H_i^B/kT,\\ &L=L(2pS^2), \quad L(x)=\coth x-1/x,\\ &\tilde{L}=L(2\tilde{p}S^2), \qquad \hat{L}=L(2\hat{p}S^2).\end{aligned}$$

The A-centered cluster shown in Fig. 17 is treated similarly. Its partition function is

$$\begin{aligned}Z_A = (\text{const})\,[&1+\mu_1^{A\,2}S_B^2(1+5L^2)+\mu_2^{A\,2}S_A^2(1+5\tilde{L}^2)\\ &+12\mu_1^A\mu_2^A S_A S_B L\tilde{L}+2\lambda_0 S_A(\mu_1^A S_B L+\mu_2^A S_A\tilde{L})\\ &+\tfrac{1}{6}\lambda_0^2 S_A^2]\,, \qquad (37)\end{aligned}$$

where $\mu_i^A=g\mu_B H_i^A/kT$.

We now have the two partition functions Z_A and Z_B whose arguments are the five molecular-field parameters λ_1^B, λ_2^B, λ_3^B, μ_1^A, and μ_2^A and the applied field parameter λ_0. From Z_A and Z_B seven different expressions for m_A and m_B are found by differentiation of $\ln Z_{A,B}$ with respect to μ_i^A, λ_i^B. From them we obtain the following five independent equations by setting equivalent magnetizations equal:

$$\begin{aligned}&\lambda_1^B L(1+\hat{L})+\lambda_2^B(2)\tilde{L}(1+\hat{L})+\lambda_3^B\tilde{L}(1+\hat{L})\\ &\quad-\mu_1^A(\tfrac{1}{3})(1+5L^2)-2\mu_2^A L\tilde{L}=\lambda_0(\tfrac{1}{3})(L-1-\hat{L})\,,\\ &\lambda_1^B(\tfrac{1}{3})(1+2L^2+3L^2\hat{L})+\lambda_2^B(2)(1+\hat{L})L\tilde{L}+\lambda_3^B(1+\hat{L})L\tilde{L}\\ &\quad-\mu_1^A(2)L-\mu_2^A(2)\tilde{L}=\lambda_0(\tfrac{1}{3})(1-L-L\hat{L})\,,\\ &\mu_1^A 2L+\mu_2^A(\tfrac{1}{3})(5\tilde{L}-1)=-\lambda_0(\tfrac{1}{3})\,, \qquad (38)\\ &\lambda_1^B L(1+\hat{L})+\lambda_2^B(\tfrac{1}{3})(6\tilde{L}\hat{L}+5\tilde{L}-1)+\lambda_3^B\tilde{L}(1+\hat{L})\\ &\quad=-\lambda_0(\tfrac{1}{3})(1+\hat{L})\,,\\ &\lambda_1^B L(1+\hat{L})+\lambda_2^B(2)\tilde{L}(1+\hat{L})+\lambda_3^B(\tfrac{1}{3})(3\tilde{L}\hat{L}+2\tilde{L}-1)\\ &\quad=-\lambda_0(\tfrac{1}{3})(1+\hat{L})\,.\end{aligned}$$

From the experimental values of Sec. VII B, the ratios $\hat{p}/p=J_{BB'}/J_{AB}=-2.36$ and $\tilde{p}/p=J_{AA}/J_{AB}=0.083$ are obtained and used in the functions $\hat{L}$ and $\tilde{L}$ in Eqs. (38). With $\lambda_0=0$, nonvanishing values of λ_i^B and μ_i^A are found at T_c, when the determinant of Eqs. (38) vanishes. This condition gives a nonlinear equation in the variable $p=J/kT$. Numerical solution of this equation yields $kT_c=1.95(-2J)=1.95J_{AB}$ or $T_c=135\,^\circ$K, quite close to the experimental value, 139 °K. Also, the dependence of T_c on the second-neighbor exchange constant was computed, for the fixed ratio $J_{BB'}/J_{AB}=-2.36$ and is shown in Fig. 18. The dependence is quite marked, and our approximate ratio of $\delta=J_{AA}/J_{AB}$ does give a value for T_c very close to the experimental result.

If $\lambda_0\neq 0$, the set of linear equations (38) is solved for the molecular-field parameters, and the sublattice magnetizations m_A and m_B can be found for $T>T_c$. With the same value of $H_0=6400$ G used in the NMR experiment,[55] these results of the BPW calculation are shown in Fig. 19. The NMR re-

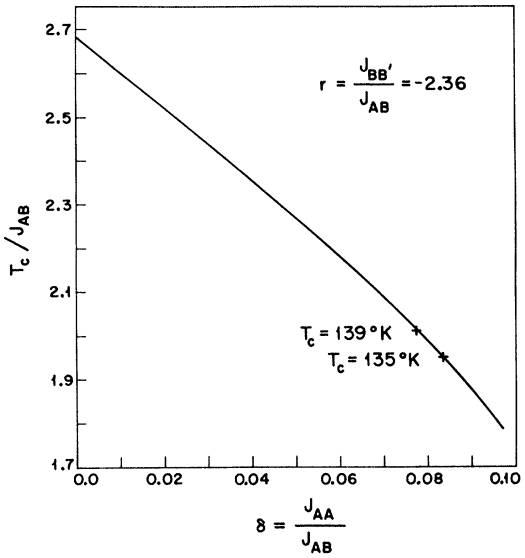

FIG. 18. Normalized ordering temperature (T_c/J_{AB}) as a function of second-neighbor interaction (J_{AA}/J_{AB}) in $RbNiF_3$ for $J_{BB'}/J_{AB} = -2.36$ calculated by the classical BPW method.

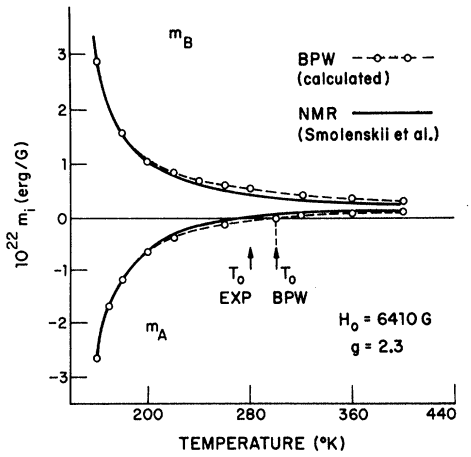

FIG. 19. Sublattice magnetizations as a function of temperature in $RbNiF_3$ determined from NMR experiments (data duplicated from Ref. 15) and classical BPW calculations.

sults shown are reproductions of the data of Ref. 55. These BPW calculations give absolute sublattice magnetizations, and neither the amplitude nor temperature scale has been normalized. There are no adjustable parameters in these final calculations, and the classical BPW method does indeed give good agreement with experiment, using the exchange constants found experimentally. In view of the approximate treatment of the second-neighbor interactions in both the spin-wave and BPW analyses, this agreement may be somewhat fortuitous. However, all of the results for T_c, T_0, and $m_{A,B}$ are quite consistent, which does increase the evidence for the accuracy of the exchange constants found for $RbNiF_3$.

IX. DISCUSSION AND COMPARISON WITH OTHER MEASUREMENTS

A. $KNiF_3$

The two-magnon Raman spectrum obtained by Fleury[4] for $RbMnF_3$ was in good agreement with the Green's-function theory. In Fig. 20 the theoretical curve for $S = \frac{5}{2}$ is compared with that for $S = 1$ as a function of normalized energy, with $\Delta = 0$. Although both have the same qualitative shape and asymmetry, the quantitative differences, such as the peak position and amplitude relative to the X point, are clearly seen. Since the experimental results in both cases are in excellent agreement with theory, the validity of the Green's-function theory is confirmed, particularly for the decoupling scheme at the heart of the treatment. This decoupling was shown to be most plausible for $S = \frac{1}{2}$, and is evidently valid over a wide range of spin values.

In terms of absolute energy shifts, the difference between the two cases is striking, because of the much stronger exchange interaction in $KNiF_3$. The two-magnon shift of ~ 850 cm^{-1} is also much larger than that reported for MnF_2,[72] FeF_2,[73] and NiF_2.[4,28] The nearest comparable two-magnon shift of ~ 510 cm^{-1} is seen in $RbNiF_3$, in which the same type of $Ni^{2+} - F - N^{2+}$ superexchange occurs.

The question now arises as to how consistent the present experimental value for $J = (102.2 \pm 1.2)$ °K is with values found by other means. Further, how does the consistency of the results compare for the two cases of $KNiF_3$ and $RbMnF_3$, the best examples to date of the interacting magnon situation? For the latter case, the theoretical Raman spectrum was computed using the exchange constant found from inelastic-neutron-scattering measurements.[74]

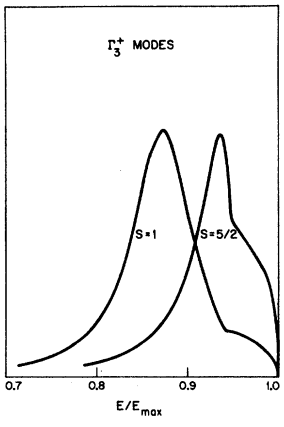

FIG. 20. Comparison of two-magnon spectra in antiferromagnetic perovskites with $S = 1$ and $S = \frac{5}{2}$, as a function of normalized energy.

Thus the two scattering experiments give the same result. No such other direct measurement exists for $KNiF_3$, and J has had to be determined indirectly from magnetic properties such as the susceptibility, Néel temperature, and paramagnetic Curie temperatures.

Analysis of the macroscopic magnetic behavior[27,75–77] and magnon-assisted infrared-absorption experiments[78] has yielded estimates of J ranging from 86 to 110 °K, with the high-temperature expansion determination of kT_N/J giving 88 °K.[27] This is considered to be a relatively reliable method, and for both $RbMnF_3$ [74] and $KMnF_3$ [79] gives results within 4% of the neutron- and Raman-scattering measurement of J. It is somewhat puzzling why there is a 13% discrepancy between the Raman-scattering and high-temperature expansion results in $KNiF_3$.

One factor which may be important in this discrepancy is the difference in spin between the Ni and Mn compounds. This may enter in either the accuracy of the high-temperature expansion method, which does not seem likely, or possibly in the additional effects of magnon-magnon interactions which occur in higher order even in the single-magnon dispersion relations. Oguchi[80] finds a multiplicative factor of $1+0.097/2S$ for the one-magnon energy in the simple-cubic antiferromagnet. The correction would be 2% for $S=\frac{5}{2}$, but increases to 5% for $S=1$. The latter correction would lower the value obtained for J in $KNiF_3$ to the point where it agreed as well with the Néel temperature results as $KMnF_3$ and $RbMnF_3$. However, this interaction factor is not definitely established. In fact, according to Korringa,[81] the correction for $S=\frac{1}{2}$ should be wave-vector dependent, and for zone-edge magnons, which are most important in two-magnon scattering, should decrease as $1-\Delta M_S/M_S$, where ΔM_S is the zero-point sublattice magnetization deviation. Presumably, either correction could be applied in an approximate manner to the two-magnon scattering problem, but since the theories are contradictory and unproven, neither factor has been included. If the wave-vector-independent correction is applied, then within the framework of the spin-wave theory this is only a small scaling factor for the exchange constant which presumably remains the same in all measured spin-wave properties.

Another factor which should be noted in the comparison of various values of exchange constants is the possible variation of J with temperature due, for example, to lattice expansion. Thus one might expect exchange constants obtained from low-temperature scattering or susceptibility measurements to vary from those found by analyses of ordering temperatures. However, in the case of $KNiF_3$, there does not seem to be such a systematic cause for different values of J.

B. K_2NiF_4

Fortunately, in the case of K_2NiF_4 there are available some recent, very interesting, and accurate measurements of both elastic[30,35] and inelastic[36] neutron scattering over a wide temperature range. The main conclusions of these experiments are that K_2NiF_4 does indeed behave like a [2] antiferromagnet. In cooling from high temperatures, the spin correlations in the NiF_2 planes become increasingly long range, and [2] order occurs at 97.1 °K (with additional [3] order setting in as well). Throughout the low-temperature range in the ordered state the magnons were found to have no observable dispersion in the c-axis direction, confirming their [2] behavior.

We have assumed that at the second- and third-nearest-neighbor intraplanar and all interplanar interactions are zero, and have found a value of (110.9 ± 3.0) °K for the nearest-neighbor exchange constant. From the inelastic-neutron-scattering measurements[36] at 5 °K, the simple one-magnon dispersion relation was best fitted over the entire Brillouin zone with $J=9.68\pm0.03$ meV $=(112.3\pm0.4)$ °K. More precisely, the analysis yielded

$$J\left(1-\frac{J_2+2J_3}{J_1}\right)=(112.3\pm0.4)\ ^\circ\mathrm{K},$$

with a least-squares fit giving $J_2+2J_3=0$, but J_1 and J_2+J_3 strongly correlated. Here, J_2 and J_3 are the second- and third-neighbor intraplanar exchange constants. Although not a major factor in the neutron-scattering analysis, the value of the anisotropy parameter found from antiferromagnetic resonance is given as $H_A=0.073$ meV $=0.85$ °K.

These results are in excellent agreement with the nearest neighbor [2] assumptions used in the theoretical treatment of the Raman scattering, and the values of the intraplanar nearest-neighbor exchange constants found from the two experiments are remarkably close. If the anisotropy had been included in the Raman-scattering analysis, with $\Delta=H_A/4J\cong0.002$, the results would not have changed significantly. A measurement of the magnetic susceptibility of Ni-doped K_2MgF_4,[77] as was done for $KMgF_3$:Ni, also gave results in good agreement with Raman- and neutron-scattering data. The exchange interactions found from the cluster-model analysis were $J=(120\pm10)$ °K, the next-nearest-neighbor intraplanar constant $J_2\cong0.5$ °K, and the interplanar constant $J'\simeq0$.

Although the anisotropy is not a large factor in determining the Raman spectrum or the spin-wave energies (except near $\vec{k}=0$), it is extremely important in the basic question of [2] magnetic behavior. In fact, Mermin and Wagner[82] have shown

that a two-dimensional system cannot have long-range magnetic order without anisotropy. On the other hand, using an isotropic-interaction Heisenberg Hamiltonian and high-temperature expansions methods, Stanley and Kaplan[30a,83] have predicted a phase transition at which the magnetic susceptibility diverges as in the usual [3] case, but without long-range order occurring. The semiempirical formula of Stanley and Kaplan, which summarizes their high-temperature expansion results, is

$$\frac{kT_c}{J} = \frac{z-1}{10}\,[2S(S+1)-1] \tag{39}$$

and predicts a transition in K_2NiF_4 at about 100 °K, quite close to the actual observed [3] ordering temperatures 97.1 °K.

On the other hand, using the Heisenberg Hamiltonian with anisotropy, Lines[27] has done a spin-wave Green's-function calculation of the Néel temperature in K_2NiF_4 as a function of the exchange constant and anisotropy. From Fig. 7 of Ref. 27, using the above experimental values, we find $T_N \simeq 93$ °K, also quite close to the actual ordering temperature 97.1 °K. In this theory, since T_N is a rather sensitive function of H_A and J, it does seem remarkable that less than 1 °K of anisotropy is sufficient to give the ordering at a temperature very close to the observed one. One might suppose that the transition predicted by Stanley and Kaplan was actually occurring and was stabilized to the normal state of long-range order by an almost arbitrarily small amount of anisotropy. Partial confirmation of this hypothesis is found from the examples of K_2MnF_4 and Rb_2MnF_4. Using exchange constants found from susceptibility measurements, Breed[32] has applied Eq. (39) and calculated [2] Néel temperatures of 41.6 and 35.2 °K for these two compounds, respectively. Their measured ordering points are 45.0 and 38.5 °K, respectively, quite close to the theoretical predictions.

Another interesting feature in K_2NiF_4 which is related to its structure is the problem of zero-point spin deviations and magnon-magnon interactions which was discussed for $KNiF_3$. Because of its lower dimensionality and the fact that the Oguchi correction factor varies as $1/zS$, one might expect that the correction factor in K_2NiF_4 would be important. Breed[32] gives the magnon-energy multiplicative factor at zero temperature as $1+0.632/2zS \simeq 1.08$, and the zero-point spin deviation is similarly predicted to be larger than in the [3] system. As in $KNiF_3$, we have not included either effect because they are not within the scope of the simple Green's-function treatment of Raman scattering. It should be noted that neither the interacting two-magnon Raman-scattering theory nor the one-magnon spin-wave theory for the neutron-scattering analysis included these higher-order effects, and both gave nearly identical results. As stated above, the Oguchi energy correction, if applicable, would enter in roughly the same way for each type of spin-wave scattering measurement by scaling the parameter J, so that this agreement would be expected.

The effect of the zero-point spin deviation on the interpretation of the scattering data is not so clear. From the direct measurement of the one-magnon dispersion relation in K_2NiF_4 by neutron scattering, no wave-vector-dependent correction to the simple spin-wave model is found, and therefore the zero-point deviation correction[81] for zone-boundary magnon energies is not warranted. Another possible way in which the spin deviation factor might enter is in the decoupling of the Green's-function equations, where averages of S^z operators are taken. However, it is not obvious that this factorization and averaging with respect to nearby spin sites should give the same results as the spin average over the entire sublattice.

A final comparison for K_2NiF_4 is with the perovskite $KNiF_3$. The $Ni^{2+} - F^- - Ni^{2+}$ exchange paths are very similar in these two materials since the lattice constants a_0 differ by less than 0.008 Å,[27] with the larger spacing in $KNiF_3$ ($a_0 = 4.014$ Å at room temperature). The exchange constants as determined by the present Raman-scattering measurements are 77 cm^{-1} for K_2NiF_4 and 70.5 cm^{-1} for $KNiF_3$. The difference is far less than the 20 cm^{-1} estimated by Lines[27] and might easily be accounted for either by the difference in lattice parameters or by the difference in covalent mixing in the two compounds. According to this latter explanation by Lines, the difference in the K^+ cation environment affects the covalency of the F^- orbitals with which it interacts and hence affects the Ni^{2+} orbitals' covalency and superexchange interactions. A 10% difference between the two exchange interactions does not seem unreasonably large. It is interesting that the ratios of exchange interactions for other similarly related compounds, as given by Breed,[32] are

$$J(Rb_2MnF_4)/J(RbMnF_3) = 7.3\ °K/6.8\ °K = 1.08,$$

$$J(K_2MnF_4)/J(KMnF_3) = 8.4\ °K/7.6\ °K = 1.10,$$

remarkably close to the result for K_2NiF_4 and $KNiF_3$. In all cases, the magnetic cation separations vary by roughly the same amounts and are larger in the perovskites, which have the smaller exchange constants.

C. $RbNiF_3$

An important question which has not yet been examined in the case of $RbNiF_3$ is the effect of exciton-magnon interactions. Parkinson and Loudon[6]

have treated this problem in detail for $RbMnF_3$, and have found conclusions very similar to those for the case of magnon-magnon interactions in Raman scattering. With a similar sort of exchange interaction between the exciton and magnon, they find that the magnon sideband created by a simultaneous optical excitation on one site and a spin excitation on a neighboring site has an energy shift less than the zone-boundary magnon energy (in the Ising approximation) by an amount $JS - J'S'$, where J (J') and S (S') are the ground- (excited-) state exchange constant and spin. As in Raman scattering, the Heisenberg interaction gives a broad asymmetrical sideband, with a binding correction slightly more than that given by the Ising model.

Unfortunately, it is not possible to apply these results directly to $RbNiF_3$. The magnon sideband in $RbMnF_3$ is a satellite of a magnetic-dipole-allowed electronic transition. In $RbNiF_3$, the main absorption lines are electric dipole vibronic transitions, phonon sidebands of first-order spin- and parity-forbidden transitions. A similar situation occurs in $KNiF_3$ with, of course, only one exciton and magnon, instead of two as in $RbNiF_3$, so that we may examine the applicability of the correction factor, since we have an accurate value for J in $KNiF_3$. Several references on the optical-absorption spectrum and its interpretation are available able.[84-87] The transition of interest is from $^3A_{2g} \rightarrow {}^1E_g$ at an energy near 15 000 cm^{-1} at low temperature, with a magnon sideband 390 cm^{-1} from this line. The noninteracting situation, with $J \cong 70$ cm^{-1}, would give a shift of 420 cm^{-1}. Since $S' = 0$ in the singlet excited state, the Ising correction would give a shift of 350 cm^{-1}. We see that although some binding occurs, it is less than half of the Ising prediction, and probably even farther from the Heisenberg result. Since the theoretical prediction for the exciton-magnon interaction in $KNiF_3$ is not accurate, there is no reason to expect that it would be any more reliable in the more complex case of $RbNiF_3$. The maximum possible correction would be a decrease of the expressions for the A and B absorption sideband shifts by one unit of J_{AB}, and as indicated in $KNiF_3$, the correction is probably much less. Because of this uncertainty and complexity, we have not included the exciton-magnon binding effects in the analysis, although they might be as important as the second-neighbor interactions in the preceding evaluation of the exchange constants.

Another point which is not clear is the absence of other two-magnon Raman lines. It seems plausible to expect only combinations of magnons on opposite sublattices to contribute to the scattering, at least at low temperatures, because of the nature of the $\vec{S}\cdot\vec{S}$ pair interaction, which will have much smaller matrix elements between pairs of nearly parallel neighboring B spins than for neighboring antiparallel A and B spins. Moreover, for density-of-states reasons, we also expect zone-edge magnons to dominate in the scattering, so that of all possible two-magnon contributions, it seems likely that two main possibilities exist: one zone-edge A-lattice magnon near the K-point energy, about $6J_{AB}$, and either of the two B-lattice magnons with energy near $3J_{AB}$ or $3J_{AB} + 2|J_{BB'}|$. The latter combination is observed, and one might expect to observe scattering from the former also, but experimentally this is not see. Because of the additional interactions present in $RbNiF_3$, and the complexity of the lattice structure, it is extremely difficult to write a Raman Hamiltonian and use the Green's-function method as in $KNiF_3$. However, we may postulate that a similar symmetry restriction comes into play for a uniform-type mode which could decrease the intensity of the lower-energy magnon pair. A direct way of verifying this argument is, of course, to carry out a Green's-function calculation with some assumptions about the Raman Hamiltonian, for example, that only $\vec{S}_A \cdot \vec{S}_B$ scattering mechanisms are present, and perhaps a simplification in the spin Hamiltonian, neglecting second-neighbor interactions. Even this, however, is a formidable task. First, we expect that it will be necessary to know the perfect crystal, or noninteracting, two-magnon Green's functions. For each general $\vec{k}$, these have to be found by diagonalizing the 6×6 spin-wave matrix, and then the appropriate summation over all $\vec{k}$ must be taken. Even assuming that these free-magnon functions are known, a further complication comes from the additional Green's function between sites on different sublattices which must be found, and which will at best lead to third-order coupled equations for these functions.

In an attempt to avoid some of these difficulties, an *ab initio* Green's-function calculation for the Ising model was tried for a simple three-sublattice analog of $RbNiF_3$ with one A and two B sites per unit cell. Starting from an Ising Hamiltonian, and a Raman Hamiltonian with only $\vec{S}_A \cdot \vec{S}_B$ terms, the same Green's-function calculation as in $KNiF_3$ was carried out. For all the free Green's functions, a simple pole with energy $9J_{AB} + |J_{BB'}|$ appeared, which is the energy of an A-lattice zone-edge magnon and the average of two B-lattice magnons. Thus, as might be expected, we see that the Ising model cannot contain the information about the phases of the B-site excitations, which is the essential difference between the types of B-lattice magnons. For this reason, we have estimated the two-magnon correction energy in the Ising-like or flat-band limit, after computing

the free-magnon dispersion relations from the Heisenberg Hamiltonian.

The temperature dependence of the Raman shift can be described qualitatively in terms of a simple-cluster theory. At the zone edge, the magnon energies are nearly equal to those found by treating the spin excitations as being localized. Computing the energy of a spin excitation in the effective field of the neighboring spins, we obtain $E(A \text{ magnon}) \simeq 6J_{AB}\langle S_B^z\rangle + 6J_{AA'}\langle S_A^z\rangle$ and $E(B \text{ magnon}) \simeq 2|J_{BB'}| - 3J_{AB}\langle S_A^z\rangle - 9J_{BB}\langle S_B^z\rangle$, for a ΔS, $\Delta M_s = 1$ transition for the coupled B-B pair. In this approximation, the total Raman energy consists of one part proportional to the sublattice magnetizations, and another part, proportional to $2|J_{BB'}|$, which will vary much more slowly with temperature as the $S=1$ and $S=0$ pair levels become populated above T_c. A rough correction for the two-magnon binding is obtained by subtracting an energy $\approx J_{AB}$ from the total Raman energy.

According to this molecular-field-type model, the Raman energy should abruptly change to the value $\sim 2|J_{BB'}|$ at T_c, since only the B-B clusters persist above T_c. Instead, the observed Raman shift continues to decrease with temperature in a manner which suggests the presence of short-range order for which $\langle \vec{S}_A \cdot \vec{S}_B \rangle$ is not zero, although $\langle \vec{S}_A \rangle \cdot \langle \vec{S}_B \rangle$ may vanish. Just above T_c, this nearest A-B neighbor correlation may be estimated from the Raman shift. Assuming that the average correlation for second neighbors is negligible at T_c, and including a binding correction, $E_{\text{Raman}} \simeq -8J_{AB} \times \langle \vec{S}_A \cdot \vec{S}_B \rangle + 2|J_{BB'}|$. E_{Raman} is ~ 400 cm^{-1} at T_c, and using the derived values of the exchange constants, we find

$$\langle \vec{S}_A \cdot \vec{S}_B \rangle_{T_c} \simeq -0.47 .$$

A similar argument for $KNiF_3$ just above T_N gave

$$\langle \vec{S}_i \cdot \vec{S}_{j+n} \rangle_{T_N} \simeq -0.52 ,$$

which is in good qualitative agreement for the same type of correlation in $RbNiF_3$.

This short-range-order persistence may also be significant in other results such as apparent ground-state energy shifts due to magnetic ordering observed in optical absorption. Assuming that the B-B pairs are ordered at T_c, the A- and B-site shifts from a molecular-field model are

$$\Delta E_A = 6J_{AB} - 6J_{AA} = 264 \text{ cm}^{-1}$$

and

$$\Delta E_B = 3J_{AB} - 9J_{BB} = 108 \text{ cm}^{-1} .$$

These are well above the measured values,[64] 170 and 50 cm^{-1}, respectively. However, if these computed values are multiplied by 0.53 to estimate the effects of short-range order still present at T_c, the shifts going from T_c to 0 °K become 140 and 57 cm^{-1}, much closer to the measured values.

From the investigation of $RbNiF_3$, it is possible to compare the experimental results with those of $KniF_3$ and K_2NiF_4. This is instructive because all three compounds have similar Ni-F-Ni configurations and exchange interactions. In the perovskite $KNiF_3$ and layered K_2NiF_4, the nearest-neighbor exchange constants were 70.5 and 77 cm^{-1}, respectively. Such similarity in the strength of the antiferromagnetic Ni-F-Ni superexchange interaction is expected since the Ni-Ni distances differ by about 0.05 Å and the spin environments are quite similar.

From these considerations one might also expect the 180° Ni-F-Ni interaction in $RbNiF_3$ to be about the same as in the potassium compounds. Qualitatively, this is true, since the interaction is strong and antiferromagnetic. However, the corresponding exchange constant is 48 cm^{-1}, roughly 30% smaller than that in $KNiF_3$. Recent x-ray analysis[88,89] of $RbNiF_3$ has measured the atomic positions accurately enough to demonstrate some differences from $KNiF_3$ which may account for the smaller size of J_{AB}. The measurements by Arnott and Longo[89] show that the A-B distance is 4.02 Å, slightly larger than the perovskite value, 4.014 Å,[45] and that the intermediate F^- ion lies 0.12 Å closer to the B site than the A site. Also, the bond angle is 178.2°, less than the 180° cubic perovskite angle. These considerations, as well as the unknown differences caused by the Rb^+ ions compared to K^+, found in the two simpler fluorides, could account for a reduction of the antiferromagnetic exchange in $RbNiF_3$.

Another point of comparison between $RbNiF_3$ and the potassium nickel fluorides is the second-nearest-neighbor exchange constant which occurs via two intermediate F^- ions. Experimentally, we have found that this parameter is 8% of the antiferromagnetic exchange constant, although this is a very rough average and could easily be an overestimate by a factor of 2. Even though the molecular-field analysis of Shafer *et al.*[48] was inadequate in that it could not be related quantitatively to microscopic exchange parameters, nevertheless a very large and antiferromagnetic intralattice interaction was found which could only arise from second- and further-neighbor interactions. Our findings are consistent with the sign of this interaction, although with a very much reduced second-neighbor exchange constant.

In comparing this result in $RbNiF_3$ with $KNiF_3$ and K_2NiF_4 there is one further point to note. One-magnon neutron scattering has shown that the distant-neighbor interactions in K_2NiF_4 are negligible, and the Raman-scattering results for $KNiF_3$ are also consistent with a nearest-neighbor inter-

action model. Therefore, the experimental evidence is that in these compounds the second-neighbor exchange [$J(2nn)$] is unimportant, even though the geometrical superexchange paths seem to be similar to some of those in $RbNiF_3$. It is quite difficult to offer any *a priori* explanations for the relative sizes of $J(2nn)$ in these compounds. Another example of such difficulties is given by $RbMnF_3$ and $KMnF_3$, which are also antiferromagnetic perovskites ($KMnF_3$ having a very slight tetragonal distortion) with very similar nearest-neighbor exchange constants. In $RbMnF_3$, neutron scattering shows no evidence of $J(2nn)$, which does exist in $KMnF_3$ and is 3% of the first-neighbor interaction.

It is worth pointing out that $RbNiF_3$ offers the unusual opportunity of measuring in one crystal both 90° and 180° exchange constants for the Ni^{2+} ion. The signs of these constants and, roughly, their relative magnitudes are in reasonable agreement with expectations from the Goodenough-Kanamori rules.[55,57] The exchange constants in the isomorphic crystal $CsMnF_3$ have also been determined.[90] Both the 90° and 180° exchange interactions in this crystal are antiferromagnetic. The difference between these compounds is explained, in the Goodenough-Kanamori theory, by the different occupancy in the Mn^{2+} and Ni^{2+} of the e_g and t_{2g} electronic orbitals.

ACKNOWLEDGMENTS

The authors express their thanks to T. A. Kaplan, H. E. Stanley, R. W. Davies, J. Longo, and J. B. Goodenough for helpful discussions, A. Mooradian for use of his experimental apparatus for part of this work, L. J. Small for help in growing the crystal samples, and Susan Landon and Nancy Brine for assistance with computer programming. We also thank P. A. Fleury and R. J. Birgeneau for interesting conversations about Raman and neutron scattering in K_2NiF_4.

---

†Work sponsored by the Department of the Air Force.

*Paper based in part on the thesis submitted by S. R. Chinn in partial fulfillment of the requirements of the Ph. D. degree at the Massachusetts Institute of Technology.

‡Present address: Hewlett-Packard Co., Palo Alto, Calif.

[1]R. J. Elliott, M. F. Thorpe, G. Imbusch, R. Loudon, and J. B. Parkinson, Phys. Rev. Letters 21, 147 (1968).

[2]M. F. Thorpe and R. J. Elliott, in *Light Scattering Spectra of Solids*, edited by G. B. Wright (Springer-Verlag, New York, 1969), p. 199; M. F. Thorpe, Ph. D. thesis, Oxford University (unpublished).

[3]R. J. Elliott and M. F. Thorpe, J. Phys. C 2, 1630 (1969).

[4]P. A. Fleury, Phys. Rev. Letters 21, 151 (1968); in *Light Scattering Spectra of Solids*, edited by G. B. Wright (Springer-Verlag, New York, 1969), p. 185.

[5]A preliminary report on two-magnon scattering in this material appears in S. R. Chinn, H. J. Zeiger, and J. R. O'Connor, J. Appl. Phys. 41, 894 (1970).

[6]J. B. Parkinson and R. Loudon, J. Phys. C 1, 1568 (1968).

[7]J. B. Parkinson, J. Appl. Phys. 40, 993 (1969).

[8]T. Tonegawa, Progr. Theoret. Phys. (Kyoto) 41, 1 (1969).

[9]S. R. Chinn and H. J. Zeiger, Phys. Rev. Letters 21, 1589 (1968).

[10]S. R. Chinn, H. J. Zeiger, and J. R. O'Connor, J. Appl. Phys. 40, 1603 (1969).

[11]P. A. Fleury, J. M. Worlock, and H. J. Guggenheim, Phys. Rev. 185, 738 (1969).

[12]F. G. Bass and M. I. Kaganov, Zh. Eksperim. i Teor. Fiz. 37, 1390 (1959) [Soviet Phys. JETP 10, 986 (1960)].

[13]R. J. Elliott and R. Loudon, Phys. Letters 3, 189 (1964).

[14]Y. R. Shen, J. Appl. Phys. 38, 1490 (1967).

[15]T. Moriya, J. Phys. Soc. Japan 23, 490 (1967).

[16]T. Moriya, J. Appl. Phys. 39, 1042 (1968).

[17]P. A. Fleury and R. Loudon, Phys. Rev. 166, 514 (1968).

[18]See, for example, C. Kittel, *Quantum Theory of Solids* (Wiley, New York, 1963), p. 58.

[19]See, for example, D. N. Zubarev, Usp. Fiz. Nauk 71, 71 (1960) [Soviet Phys. Usp. 3, 320 (1960)]; S. V. Tyablikov, *Methods in the Quantum Theory of Magnetism*, translated by H. A. Tybulewicz (Plenum, New York, 1967).

[20]S. R. Chinn, Ph. D. thesis, MIT, 1970 (unpublished).

[21]T. Wolfram and J. Callaway, Phys. Rev. 130, 2207 (1963).

[22]M. Yussouff and J. Mahanty, Proc. Phys. Soc. (London) 85, 1223 (1965).

[23]D. Hone, H. Callen, and L. R. Walker, Phys. Rev. 144, 283 (1966).

[24]M. F. Thorpe, J. Appl. Phys. 41, 892 (1970).

[25]P. L. Richards, J. Appl. Phys. 34, 1237 (1963).

[26]D. T. Teaney, M. J. Freiser, and R. W. H. Stevenson, Phys. Rev. Letters 9, 212 (1962).

[27]M. E. Lines, Phys. Rev. 164, 736 (1967).

[28]P. A. Fleury, Phys. Rev. 180, 591 (1969).

[29]An account of these results is contained in S. R. Chinn, thesis, MIT, 1970 (unpublished). See also P. A. Fleury and H. J. Guggenheim, Phys. Rev. Letters 24, 1346 (1970).

[30]R. J. Birgeneau, H. J. Guggenheim, and G. Shirane, Phys. Rev. Letters 22, 720 (1969).

[30a]*Footnote added in proof.* H. E. Stanley and T. A. Kaplan, Phys. Rev. Letters 17, 912 (1966).

[31]D. J. Breed, Physica 37, 35 (1967).

[32]D. J. Breed, Ph. D. thesis, University of Amsterdam, 1969 (unpublished).

[33]V. J. Folen, J. J. Krebs, and M. Rubinstein, J. Appl. Phys. 40, 1370 (1969).

[34]W. G. Maisch, J. Appl. Phys. 40, 1330 (1969).

[35]R. J. Birgeneau, J. Skalyo, Jr., and G. Shirane, J. Appl. Phys. 41, 1303 (1970).

[36]J. Skalyo, Jr., G. Shirane, R. J. Birgeneau, and H. J. Guggenheim, Phys. Rev. Letters 23, 1394 (1969).

[37]K. G. Srivastava, Phys. Letters 4, 55 (1963).
[38]J. S. Tiwari, A. Mehra, and K. G. Srivastava, Japan J. Appl. Phys. 7, 506 (1968).
[39]E. P. Maarschall, A. C. Botterman, S. Vega, and A. R. Miedema, Physica 41, 473 (1969).
[40]M. E. Lines, J. Appl. Phys. 40, 1352 (1969).
[41]J. B. Parkinson, J. Phys. C 2, 2112 (1969).
[42]I. S. Gradshteyn and I. M. Ryzhik, *Tables of Integrals, Series and Products*, translated by A. Jeffrey (Academic, New York, 1965).
[43]L. Robin, *Tables Numériques des Fonctions Associées de Legendre* (Collection Technique et Scientifique du Centre National d'Etudes des Télécommunications, Paris, 1959).
[44]G. A. Smolenskii, V. M. Yudin, P. P. Syrnikov, and A. B. Sherman, Zh. Eksperim. i Teor. Fiz. Pis'ma v Redaktsiyu 3, 416 (1966) [Soviet Phys. JETP Letters 3, 271 (1966)].
[45]G. A. Smolenskii, V. M. Yudin, P. P. Syrnikov, and A. B. Sherman, Fiz. Tverd. Tela 8, 2965 (1966) [Soviet Phys. Solid State 8, 2368 (1967)].
[46]R. D. Burbank and H. T. Evans, Jr., Acta Cryst. 1, 330 (1948).
[47]J. A. Kafalas and J. M. Longo, Mater. Res. Bull. 3, 501 (1968).
[48]M. W. Shafer, T. R. McGuire, B. E. Argyle, and G. J. Fan, Appl. Phys. Letters 10, 202 (1967).
[49]E. I. Golovenchitz, A. G. Gurevich, and V. A. Sanina, Zh. Eksperim. i Teor. Fiz. Pis'ma v Redaktsiyu 3, 408 (1966) [Soviet Phys. JETP Letters 3, 266 (1966)].
[50]A. T. Starovoitov, V. I. Ozhogin, and V. A. Bokov, Fiz. Tverd. Tela 10, 1553 (1968) [Soviet Phys. Solid State 10, 1228 (1968)].
[51]R. V. Pisarev, I. G. Sinii, and G. A. Smolenskii, Zh. Eksperim. i Teor. Fiz. Pis'ma v Redaktsiyu 5, 96 (1967) [Soviet Phys. JETP Letters 5, 79 (1967)].
[52]R. V. Pisarev, I. G. Sinii, and G. A. Smolenskii, Fiz. Tverd. Tela 9, 3149 (1967) [Soviet Phys. Solid State 9, 2482 (1968)].
[53]G. A. Smolensky, R. V. Pisarev, M. P. Petrov, V. V. Moskalev, I. G. Sinii, and V. M. Judin, J. Appl. Phys. 39, 568 (1968).
[54]G. A. Smolensky, M. M. Petrov, V. V. Moskalev, V. S. Kasperovich, and E. V. Jirnova, Phys. Letters 25A, 519 (1967).
[55]G. A. Smolenskii, M. P. Petrov, V. V. Moskalev, V. S. L'vov, V. S. Kasperovich, and E. V. Zhirnova, Fiz. Tverd. Tela 10, 1305 (1968) [Soviet Phys. Solid State 10, 1040 (1968)].
[56]J. B. Goodenough, *Magnetism and the Chemical Bond* (Interscience, New York, 1963).
[57]P. W. Anderson, in *Solid State Physics*, edited by F. Seitz and D. Turnbull (Academic, New York, 1963), Vol. 14, p. 99.
[58]A. Brooks Harris, Phys. Rev. 132, 2398 (1963).
[59]W. Brinkman and R. J. Elliott, J. Appl. Phys. 37, 1457 (1966).
[60]W. F. Brinkman and R. J. Elliott, Proc. Roy. Soc. (London) A274, 343 (1966).
[61]J. C. Slater, *Quantum Theory of Molecules and Solids* (McGraw-Hill, New York, 1965), Vol. 2.
[62]W. W. Holloway, Jr., and M. Kestigian, Phys. Rev. Letters 15, 17 (1965).
[63]R. V. Pisarev, Fiz. Tverd. Tela 8, 2300 (1966) [Soviet Phys. Solid State 8, 1836 (1967)].
[64]G. Zanmarchi and P. F. Bongers, Solid State Commun. 6, 27 (1968).
[65]J. Tylicki, W. M. Yen, J. P. van der Ziel, and H. J. Guggenheim, Phys. Rev. 187, 758 (1969).
[66]T. A. Kaplan, Phys. Rev. 119, 1460 (1960).
[67]J. S. Smart, *Effective Field Theories of Magnetism* (Saunders, Philadelphia, 1966).
[68]P. W. Kasteleijn, Ph. D. thesis, Lorentz Institute, Leiden University, 1956 (unpublished).
[69]P. W. Kasteleijn and J. van Kranendonk, Physica 22, 317 (1956).
[70]H. A. Brown and J. M. Luttinger, Phys. Rev. 100, 685 (1955).
[71]H. A. Brown, Phys. Chem. Solids 26, 1379 (1965).
[72]P. A. Fleury, S. P. S. Porto, and R. Loudon, Phys. Rev. Letters 18, 658 (1967).
[73]P. A. Fleury, S. P. S. Porto, L. E. Cheesman, and H. J. Guggenheim, Phys. Rev. Letters 17, 84 (1966).
[74]C. G. Windsor and R. W. H. Stevenson, Proc. Phys. Soc. (London) 87, 501 (1966).
[75]K. Hirakawa, K. Hirakawa, and T. Hashimoto, J. Phys. Soc. Japan 15, 2063 (1960).
[76]T. Hashimoto, J. Phys. Soc. Japan 18, 1140 (1963).
[77]Y. Yamaguchi and N. Sakamoto, J. Phys. Soc. Japan 27, 1444 (1969).
[78]A. Tsuchida, J. Phys. Soc. Japan 21, 2497 (1966).
[79]S. J. Pickart, M. F. Collins, and C. G. Windsor, J. Appl. Phys. 37, 1054 (1966).
[80]T. Oguchi, Phys. Rev. 117, 117 (1960).
[81]J. Korringa, Phys. Rev. 125, 1972 (1962).
[82]N. D. Mermin and H. Wagner, Phys. Rev. Letters 17, 1133 (1966).
[83]H. E. Stanley, J. Appl. Phys. 40, 1546 (1969).
[84]K. Knox, R. G. Shulman, and S. Sugano, Phys. Rev. 130, 512 (1963).
[85]S. Sugano and Y. Tanabe, Tech. Rept. Inst. Solid State Phys. Univ. Tokyo A71, 1 (1963).
[86]J. Ferguson, H. J. Guggenheim, and D. L. Wood, J. Chem. Phys. 40, 822 (1964).
[87]J. Ferguson and H. J. Guggenheim, J. Chem. Phys. 44, 1095 (1966).
[88]D. Babel, Z. Anorg. Allgem. Chem. 369, 1171 (1969).
[89]R. J. Arnott and J. M. Longo, J. Solid State Chem. (to be published).
[90]M. H. Seavey, Phys. Rev. Letters 23, 132 (1969).